CITY UNIVERSITY LONDON EST 1894

A hybrid model for simulating rogue waves in random seas on a large temporal and spatial scale

Jinghua Wang, Q.W. Ma*, S. Yan

School of Mathematics, Computer Science and Engineering, City University London, EC1V 0HB, UK

Abstract

A hybrid model for simulating rogue waves in random seas on a large temporal and spatial scale is proposed in this paper. It is formed by combining the derived fifth order Enhanced Nonlinear Schrödinger Equation based on Fourier transform, the Enhanced Spectral Boundary Integral (ESBI) method and its simplified version. The numerical techniques and algorithm for coupling three models on time scale are suggested. Using the algorithm, the switch between the three models during the computation is triggered automatically according to wave nonlinearities. Numerical tests are carried out and the results indicate that this hybrid model could simulate rogue waves both accurately and efficiently. In some cases discussed, the hybrid model is more than 10 times faster than just using the ESBI method, and it is also much faster than other methods reported in literature.

Keywords: Hybrid model. Rogue wave. Random wave. Large scale. FFT

1   Introduction

1.1 Background

The study of surface ocean waves has a long history [1, 2, 3, 4, 5], however, rogue waves didn't draw extensive attentions until recent decades. The rogue waves are extraordinarily large water waves in ocean and have been recognized as great threats to the safety of offshore structures [6, 7]. It is commonly defined as the wave with maximum wave height exceeding 2 times of significant wave height (H_s) and/or the maximum wave amplitude exceeding 1.25 H_s [8]. Their occurrence is in fact more frequent than rare [9]. The rogue waves might be caused by many factors, such as the energy focusing due to the seabed geometry, wind-wave interaction, wave-current interaction, modulation instability, etc., which have been discussed and reviewed by researchers [9, 10].

The most distinguished feature of rogue wave is its transience, which means that it can happen and disappear very rapidly [9]. Due to that reason, it cannot be modeled by using steady wave theories, e.g., Stokes waves [4], cnoidal waves [11] or solitary wave [12], which describe such waves with permanent profiles not evolving in time. Furthermore, due to the rapid appearance of rogue waves and the persistently changing sea state, the statistical stationarity condition also breaks down [9]. Therefore, studies need be carried out in time domain to explore the physics of rogue waves.

Meanwhile, rogue waves can also have large steepness and strong nonlinearity. As pointed out by Kriebel [13, 14], Onorato, et al. [15] and Phillips [16], the linear and second

---

order wave theories significantly underestimate the rogue wave dynamics, thus third or higher order or fully nonlinear theories are required [16], which also has been confirmed by numerical simulations in [17, 18]. In addition, the nonlinearities of rogue waves are so strong that sometimes breaking occurs in many occasions. In order to deal with these cases, the Navier-Stokes (NS) equations may be numerically solved, as has been done by, e.g., Harlow and Welch [19] and Hirt and Nichols [20]. However, this class of methods is so inefficient that it is impossible to be employed for a large scale simulation even with the very powerful computer available today.

On top of that, the studies on rogue waves have already been carried out extensively on the local scale, such as rogue wave interaction with wind [21, 22], current [23, 24] and structures [25, 26], etc. The work significantly contributed to our understanding of the local effects of rogue waves over a short window of time. However, the formation of rogue waves in random seas is not fully explained by using the knowledge of the local effects [9]. To fully understand the formation for rogues, simulations of wave fields in large and long time scale with sufficient nonlinear effects are needed as indicated by [27].

The statistical studies have suggested that the rogue waves usually have exceedance probabilities ranging from 10^{-3} to 10^{-5} [10]. Unquestionably, it may take long duration to observe an occurrence of the rogue wave directly from random sea simulation either physically or numerically. For example, within the range of real observation, one may need to record $10^3 \sim 10^5$ individual waves to collect reliable statistics, e.g. 3000 waves based on Rayleigh distribution [9]. Most importantly, in such a way, the occurrence of the rogue waves is random and unpredictable. It may appear after a sufficient long-time evolution due to nonlinearity, thus the duration of the numerical simulation must be long enough, e.g., covering the life span of one random sea state. Duration shorter than this may not well represent the evolution of random seas. Since the real sea states averagely last for 3 hours [28], and a typical peak period $T_0 \approx 10s$ in North Sea [29, 30], the duration of the simulation may need to last as long as approximately $1000T_0$.

In addition, traditional statistical model only looks at the surface time history at a fixed location. While rogue waves can occur at arbitrary position during the nonlinear evolution, so that regional statistics must be considered [31]. According to Forristall's study on the air gap under the deck of a platform [32], the maximum crest height in the whole working area ($50\text{m} \times 50\text{m}$) is almost 20% higher than the one expected at a single point. This further addresses the importance for developing a statistical model describing wave probability over a specific area, instead of just looking at a fixed location [9]. However, very few studies on regional statistics of rogue waves have been carried out so far, although researchers are aware that higher crests appear in radar images [32]. Meanwhile, instead of directly using such statistical model, random seas may be simulated numerically so that the free surface can be obtained at every time step, which can later be used for regional statistics. To do so, the domain should be large enough to account for the possible locations where rogue waves may occur as the location of rogue waves are unpredictable. For long-crest waves, i.e., in 2D situations, a domain of $128L_0$ is used in [29]. Many attempts in literature have been made in order to develop the various simulation methods which can be employed to study the rogue

waves in a large temporal and spatial scale. A brief review on them will be given in the following subsections.

1.2 Numerical models for large scale simulations

Phase-averaged or the so called third generation wind wave models, such as WAM, SWAN, WAVEWATCH etc., have long been suggested and widely adopted in engineering and applied sciences. However, only the statistic features of the waves could be obtained, such as the peak frequency, significant wave height and so on. The space-time information of the specific wave dynamics is lost by using them, which however is very important for considering the dynamics of rogue waves for different purposes. Thus, phase-resolved models have been sought after. Among them, numerical models based on the NS equation are not computationally economical for large scale simulations as pointed out above and such applications in literatures are rare. The potential theory assumes that the fluid is inviscous and irrotational, which makes numerical simulations much faster. Therefore, we will only consider potential models in the present study to simulate non-breaking waves, and so the review below will be focused on the work related to using potential models.

1.2.1 Weakly nonlinear models

The simplified mathematical models, such as the Boussinesq, KdV, and Schrödinger equations have been widely used to study weakly nonlinear waves. The Boussinesq equation [12] and KdV equation [11] were derived by assuming small steepness and water depth to study shallow water waves. Both the equations are obtained by assuming the Ursell number $U_r = aL^2/h^3 \approx O(1)$ [33]. Thus they are mainly used for studying weakly nonlinear waves in shallow water situations. Although improved models which could be used in deep water are suggested, such as the higher order Boussinesq equation by Wei et al. [34] and. Madsen et al [35], as well as multi-layered Boussinesq model by Lynett and Liu [36], they are relatively computational expensive so that are hardly used in large scale simulations. Nevertheless, both the KdV and Boussinesq equations are only accurate when used to simulate waves in shallow and finite water depth, so that they will not be further discussed in this paper. A detailed review about the KdV and Boussinesq equation could be found in [37].

The nonlinear Schrödinger equation (NLSE) is another tool to study the dynamics of the gravity water waves in deep and finite water depth. The third order weakly nonlinear equation was first derived from the Zakharov equation [38], which is referred as the cubic NLSE (shortened as CNLSE) in this paper. Subsequently, Benny and Roskes [39], Hasimoo and Ono [40], Davey and Stewartson [41] also came up with the similar equations by using perturbation method. Based on the previous studies, Dysthe [42] extended this theory to the fourth order for narrow bandwidth waves and proposed what is referred to the Dysthe equation. Trulsen and Dysthe [43] further extended the work and derived an equation for broader bandwidth waves. Later, Trulsen et al [44] corrected the linear terms to the exact linear solution, and named their model as the fourth order Enhanced Nonlinear Schrödinger Equation (shortened as ENLSE-4 in this paper). Meanwhile, Stiassnie [45] applied the narrow bandwidth assumption to the Zakharov equation and derived the same equation as Dysthe

[42], which indicates that the Dysthe equation is a special case of the Zakharov equation. Debsarma and Das [46] used the same technique and obtained a fifth order equation called the Higher Order Dysthe Equation in terms of Hilbert transform. Similarly, by introducing Trulsen et al.'s approach [44], the linear operation of this equation could be enhanced and we refer it as the fifth order Enhanced Nonlinear Schrödinger Equation based on Hilbert transform (shortened as ENLSE-5H) in this paper.

Applications of Schrödinger type equations in large scale simulations are extensive. Dysthe et al. [47] investigated free surface evolution by directly simulating random waves based on the Dysthe equation in a domain covering 100×100 peak wave lengths for 150 peak periods. Onorato et al. [48] brought the effects of current into the CNLSE and showed that rogue waves can be generated naturally when a stable wave train enters a region of an opposing current flow based on a numerical simulation in a domain of 60 peak wave lengths lasting for 60 peak periods. In addition, Shemer et al. [49] studied the probability of rogue waves in random wave simulations based on both the CNLSE and the Dysthe equation in a domain of 77 peak wave lengths during 100 peak periods. More studies can also be found in [50, 51].

1.2.2 Fully nonlinear models

Besides, studies of rogue waves have also been carried out by using the fully nonlinear potential theory. Some papers employed Boundary Element Method (BEM) [52, 53], and others used Finite Element Method (FEM) [54, 55] or Quasi Arbitrary Lagrangian-Eulerian Finite Element Method (QALE-FEM) [26, 56]. Some of these methods can simulate waves with overturning (e.g. [53, 56]) but they are relatively expensive, so they have not been applied to modelling wave in vary large scale so far. Another category of nonlinear potential methods is based on the FFT. One of them is the Higher-Order Spectral (HOS) method proposed by West et al. [57], and subsequently by Dommermuth and Yue [58] to simulate propagating waves. This method applied the Taylor expansion of the velocity potential on the free surface with respect to vertical coordinate. It is accurate and efficient when the waves to be studied are not very steep ($\varepsilon = k_0 a_0 < 0.35$) [58]. Nicholls [59] suggested a numerical model called Spectral Continuation method to study the traveling water wave problems. The Dirichlet-Neumann operator is approximated by a limited Taylor series. Due to the fact that evaluating the higher order terms is highly recursive and impractical, they chose to use the expansions to the fifth order in practice. As a consequence, this method is incapable to capture the higher order nonlinearities and only accurate when the nonlinearities are weak. Clamond and Grue [60] suggested another method combing boundary integral equations and FFT technique in two and three dimensions. The formulations for 3D situation was later implemented and numerically tested by Fructus et al. [61] and Grue [62], named as the Spectral Boundary Integral (SBI) method. This method is recently improved and enhanced by Wang and Ma [63] in three aspects including provision of new techniques for anti-aliasing and de-singularization, and a new algorithm for automatically including or excluding integral terms involved in the method. It has been observed that the new technique can help the method being more than 35 time faster than the method without the techniques in some cases.

The method presented by Wang and Ma [63] with the new techniques will be referred as to Enhanced Spectral Boundary Integral (ESBI) method in this paper for convenience.

The FFT based fully nonlinear methods have been successfully applied in large scale simulations. Clamond et al. [64] simulated the evolution of wave groups by using the SBI method in a 2D NWT covering 128 peak wave lengths up to 2000 peak periods. Ducrozet et al. [29] had investigated the occurrence of rogue waves in 2D and 3D large open seas of 42×42 peak wave lengths for 250 peak periods by direct simulation of random waves using HOS method. Xiao et al. [65] also studied the dynamics of rogue waves in 3D NWT covering 128×128 peak wave lengths which lasts for 150 peak periods based on HOS to account for the directional spreading effects.

1.3 Issues to be addressed

As indicated above, the literature reveals that rogue waves need to be modelled in a large temporal and spatial scale with full consideration of nonlinearity. In addition, a large number of parameter studies are required to quantify the behaviors of rogue waves as shown Xiao et al. [65] and in engineering design. This inheritably demands the modelling methods to be efficient. Although versatile versions of NLSE have been suggested and are computationally efficient, they are only accurate when waves are moderate. Henderson et al. [66] simulated traveling waves based on the CNLSE and fully nonlinear Higher-Order BEM, and concluded that there was good agreement between the results of these two models only for waves with small steepness ($\varepsilon = k_0 a_0 < 0.056$). Clamond et al. [64] investigated the evolution of the envelope soliton with an initial steepness of $\varepsilon = 0.091$ using the ENLSE-4 and their fully nonlinear approach separately. Through comparing the free surface profiles, they concluded that the former was only valid for a limited period at the beginning of the simulation before rogue waves are formed, and indicated that the ENLSE-4 became inaccurate when wave steepness evolved to be $\varepsilon \geq 0.21$. Slunyaev et al. [67] have compared the analytical solution of the CNLSE with the numerical results of the Dysthe equation and the fully nonlinear Euler equations for simulating rogue waves. They concluded that the CNLSE was not accurate for waves with initial steepness $\varepsilon \geq 0.117$.

On the other hand, the fully nonlinear models are more accurate than the weakly nonlinear models for dealing with strong nonlinear waves, one should note that they are relatively more computationally expensive. It was reported, for example, by Ducrozet et al. [29] that the simulation of a 3D random sea covering 42×42 peak wave lengths and propagating for 250 peak wave periods costs 10 CPU days on a 3 GHz-Xeon single processor PC by using the fifth order High-order Spectral method! It is far longer than a sea state ($\approx 3hrs$). That indicates that the existing fully nonlinear models are not sufficiently efficient for a large scale simulation and for use in design where a large number of parameter studies may be necessary.

In summary, there is currently a lack of numerical methods which can model rogue waves in a large scale with full nonlinearity and with sufficient efficiency. In this paper, we will propose a new hybrid model coupling the models with different levels of approximations and efficiencies. The basic idea is that when waves are not steep, the simplified but efficient

models are used; only when necessary, the fully nonlinear but less efficient models are employed. In this way, one can achieve higher efficiency without loss of accuracy. The ESBI described in [63] will be selected as the fully nonlinear model. The ENLSE-5H suggested by Debsarma and Das [46], will be used as the simplified and efficient model but will be reformulated to overcome some of its drawbacks. As well known, the ENLSE is accurate only with relatively narrow bandwidth waves, but may not be accurate for broad bandwidth waves even their steepness is not very large. A proper alternation is needed to replace the ENLSE for modelling waves of broad bandwidth with moderate steepness. This will be obtained by a reduced form of the ESBI. The relevant techniques for coupling the models will be detailed in the following sections.

2   Mathematical formulations

2.1   The Spectral Boundary Integral Method

This method has been suggested by Clamond and Grue [60], Fructus et al. [61] and Grue [62], and improved by Wang and Ma [63]. So details will not be given here. However the summary of main equations is just presented for completeness. Based on the potential theory, the governing equation together with all boundary conditions are given as

$$\Delta \phi = 0 \tag{1}$$

$$\frac{\partial \eta}{\partial T} + \nabla \phi \cdot \nabla \eta - \frac{\partial \phi}{\partial Z} = 0, \quad on \quad Z = \eta \tag{2}$$

$$\frac{\partial \phi}{\partial T} + \eta + \frac{1}{2}\left(\nabla \phi \cdot \nabla \phi + \frac{\partial \phi^2}{\partial Z} \right) = 0, \quad on \quad Z = \eta \tag{3}$$

$$\frac{\partial \phi}{\partial Z} = 0, \quad Z \to -\infty \tag{4}$$

where Δ is the Laplacian and $\nabla = \partial/\partial \boldsymbol{X} = \partial/\partial X \vec{\imath} + \partial/\partial Y \vec{\jmath}$ is the horizontal gradient operator, and η is the elevation of the free surface, ϕ is the velocity potential. Among the variables in the equations above, η, $\boldsymbol{X} = (X,Y)$ and Z have been non-dimensionalized by multiplying k_0, ϕ by multiplying $\sqrt{k_0^3/g}$ and T by multiplying ω_0, where $\omega_0 = \sqrt{gk_0}$ is the representative circular frequency and g is the gravity acceleration.

In order to derive the equations for numerical simulation, the Fourier transform $F\{\}$ and the inverse transform $F^{-1}\{\}$ are employed and defined as

$$\hat{\eta}(\boldsymbol{K},T) = F\{\eta\} = \int_{-\infty}^{\infty} \eta(\boldsymbol{X},T)e^{-i\boldsymbol{K}\cdot\boldsymbol{X}}d\boldsymbol{X} \tag{5}$$

$$\eta(\boldsymbol{X},T) = F^{-1}\{\hat{\eta}\} = \frac{1}{4\pi^2}\int_{-\infty}^{\infty} \hat{\eta}(\boldsymbol{K},T)e^{i\boldsymbol{K}\cdot\boldsymbol{X}}d\boldsymbol{K} \tag{6}$$

where the wave number $\boldsymbol{K} = (\kappa, \zeta)$. Fast Fourier Transform (FFT) is adopted to perform the Fourier and inverse transform (IFFT) numerically.

The boundary conditions on the free surface could be reformulated as

$$\frac{\partial \eta}{\partial T} - V = 0 \tag{7}$$

$$\frac{\partial \tilde{\phi}}{\partial T} + \eta + \frac{1}{2}\left(|\nabla\tilde{\phi}|^2 - \frac{(V + \nabla\eta \cdot \nabla\tilde{\phi})^2}{1 + |\nabla\eta|^2}\right) = 0 \tag{8}$$

after introducing $V = \partial\phi/\partial n\sqrt{1 + |\nabla\eta|^2}$ and the velocity potential at free surface $\tilde{\phi}$. This is referred as the Dirichlet to Neumann operation. Applying Fourier transform to both the boundary conditions leading to the skew-symmetric prognostic equation

$$\frac{\partial M}{\partial T} + AM = N \tag{9}$$

where

$$M = \begin{pmatrix} KF\{\eta\} \\ K\Omega F\{\tilde{\phi}\} \end{pmatrix}, \quad A = \begin{bmatrix} 0 & -\Omega \\ \Omega & 0 \end{bmatrix}, \quad N = \begin{pmatrix} K(F\{V\} - KF\{\tilde{\phi}\}) \\ K\Omega F\left\{\frac{1}{2}\left[\frac{(V+\nabla\eta\cdot\nabla\tilde{\phi})^2}{1+|\nabla\eta|^2} - |\nabla\tilde{\phi}|^2\right]\right\} \end{pmatrix} \tag{10}$$

and the circular frequency $\Omega = \sqrt{K}$, wave number $K = |K| = \sqrt{\kappa^2 + \zeta^2}$. Then the solution is given as

$$M(T) = e^{-A(T-T_0)}\int_{T_0}^{T} e^{A(T-T_0)} N dT + e^{-A(T-T_0)} M(T_0) \tag{11}$$

where

$$e^{A\Delta T} = \begin{bmatrix} \cos\Omega\Delta T & -\sin\Omega\Delta T \\ \sin\Omega\Delta T & \cos\Omega\Delta T \end{bmatrix} \tag{12}$$

On the other hand, the boundary integral of Green's theorem based on Eq. (1) follows as

$$\iint_S \frac{1}{r}\frac{\partial\phi'}{\partial n'} dS' = 2\pi\tilde{\phi} + \iint_S \phi'\frac{\partial}{\partial n'}\frac{1}{r} dS' \tag{13}$$

where S is the area of the instantaneous free surface, the variables with the prime indicate those at source point (X', Z'), the variables without the prime are those at field point (X, Z), $r = \sqrt{R^2 + (Z' - Z)^2}$ and $R = |R| = |X' - X|$, dS' denotes the segment of $S(X', Z')$. Using $dS' = \sqrt{1 + |\nabla\eta|^2} dX'$, the above integral can be written as

$$\int_{S_0} \frac{V'}{r} dX' = 2\pi\tilde{\phi} + \int_{S_0} \tilde{\phi}'\sqrt{1 + |\nabla'\eta'|^2}\frac{\partial}{\partial n'}\frac{1}{r} dX' \tag{14}$$

where S_0 is the projection of S' to the horizontal plane. Then a variable $D = (\eta' - \eta)/R$ is introduced and the equation above is reformulated as

$$\int_{S_o} \frac{V'}{R} d\boldsymbol{X}' = 2\pi\tilde{\phi} + \int_{S_o} (\eta' - \eta)\nabla'\tilde{\phi}' \cdot \nabla' \frac{1}{R} d\boldsymbol{X}'$$
$$- \int_{S_o} \tilde{\phi}' \left[\frac{1}{(1+D^2)^{3/2}} - 1 \right] \nabla' \cdot \left[(\eta' - \eta)\nabla' \frac{1}{R} \right] d\boldsymbol{X}' \tag{15}$$
$$- \int_{S_o} \frac{V'}{R} \left(\frac{1}{\sqrt{1+D^2}} - 1 \right) d\boldsymbol{X}'$$

The velocity V can be split into four parts, i.e., $V = V_1 + V_2 + V_3 + V_4$. Each part is given by

$$V_1 = F^{-1}\left\{ KF\{\tilde{\phi}\} \right\} \tag{16}$$

$$V_2 = -F^{-1}\left\{ KF\{\eta V_1\} \right\} - \nabla \cdot (\eta\nabla\tilde{\phi}) \tag{17}$$

$$V_3 = F^{-1}\left\{ \frac{K}{2\pi} F\left\{ \int_{S_o} \tilde{\phi}' \left[1 - \frac{1}{(1+D^2)^{3/2}} \right] \frac{(\eta' - \eta) - \boldsymbol{R} \cdot \nabla'\eta'}{R^3} d\boldsymbol{X}' \right\} \right\} \tag{18}$$

$$V_4 = F^{-1}\left\{ \frac{K}{2\pi} F\left\{ \int_{S_o} \frac{V'}{R} \left(1 - \frac{1}{\sqrt{1+D^2}} \right) d\boldsymbol{X}' \right\} \right\} \tag{19}$$

where V_1 and V_2 could be estimated directly by applying the Fourier and its inverse transforms. Fructus et al. [61] has rewritten the kernel of V_4, and the dominant part could be expanded into the third order convolutions, say

$$V_4 = -\frac{K}{2} \left[KF\{\eta^2 V\} - 2F\left\{ \eta F^{-1}\{KF\{\eta V\}\} \right\} + F\left\{ \eta^2 F^{-1}\{KF\{V\}\} \right\} \right]$$
$$+ \frac{K}{2\pi} F\left\{ \int \frac{V'}{R} \left(1 - \frac{1}{\sqrt{1+D^2}} - \frac{1}{2}D^2 \right) d\boldsymbol{X}' \right\} \tag{20}$$

The calculation of the convolutions is very fast owing to the algorithm of FFT. Otherwise, the remaining integration part of V_4 and the whole expression of V_3 are estimated through numerical integration, which is the most time consuming part of the numerical method. In addition, the numerical integration is estimated at nodes $\boldsymbol{X} + \Delta\boldsymbol{X}/2$ and shifted back to regular points through Fourier interpolation in order to avoid explicit singularity for calculating the integrand in [61]. It is found that the resolution needs to be well refined in order to obtain accurate results by using this method. Grue [62] made one step further, expanded the kernels of V_3 and V_4 and wrote the dominant parts into the convolutions up to the sixth and seventh order respectively. Both the remaining integration parts of V_3 and V_4 are neglected. The numerical scheme is significantly accelerated due to the most time consuming parts are excluded. However, it is based on the assumption that the gradient parameter $D \ll 1$. If the condition is not met, such as the cases where the wave free surface is quite steep even in a local area, the integration parts can be important to the accuracy of estimating V_3 and V_4 and could not be neglected.

In the study by Wang and Ma [63], some numerical techniques on improving the

computational efficiency of this numerical model have been proposed. Firstly, a new numerical de-singularity technique was introduced. It is found that to reach the same level of accuracy, one could use much less points if the new method is applied. The second contribution of that paper was to propose a new technique to deal with anti-aliasing problem associated with FFT/IFFT. The other contribution they made was to reformulate the equation for V_3 and V_4 as

$$V_3 = V_{3,c} + V_{3,I} = \underbrace{V_3^{(1)}}_{4th} + \underbrace{V_3^{(2)}}_{6th} + \underbrace{V_{3,I}}_{integration} \tag{21}$$

$$V_4 = V_{4,c} + V_{4,I} = \underbrace{V_4^{(1)}}_{3rd} + \underbrace{V_4^{(2)}}_{5th} + \underbrace{V_4^{(3)}}_{7th} + \underbrace{V_{4,I}}_{integration} \tag{22}$$

During their simulation, the gradient of wave surface is monitored. When the waves satisfy a condition that they are moderate or their gradient is small, the velocity components will be evaluated through only estimating convolutions up to the seventh order with the integration parts neglected. The integration parts are estimated only when the condition is not met. For regular waves, the condition is $|D|_{max} \leq D_c$, where D_c can be taken as 0.5. For random waves, the condition is $max|V_3^{(3)}|/max|V| < 10^{-5}$, where $V_3^{(3)}$ is the eighth order convolution part. With the three new techniques, the method becomes much faster. It has been observed to be more than 35 time faster than the method without the techniques in some cases. The method presented by Wang and Ma [63] will be referred to as Enhanced Spectral Boundary Integral (ESBI) method in this paper for convenience.

Built on that paper, another computational efficient method may be formed, in which only the third order convolution terms, neglecting the integration terms in the vertical velocity, i.e., $V = V_1 + V_2 + V_4^{(1)}$ are considered. The difference between this approximate approach and the ESBI lies in the vertical velocity estimation. All others, including the prognostic equation and full nonlinear free surface conditions, are the same as the ESBI. It is expected that this approximate approach will be as accurate as the ESBI when the waves are not strongly nonlinear. This approximate approach will be referred as the Quasi Spectral Boundary Integral (QSBI) method in this paper for convenience. Both the QSBI and ESBI methods are solved by using embedded fifth order Runge-Kutta method with adaptive time step. The details of the numerical scheme could be found in [63]. The QSBI will be formed as a part of the hybrid method developed in this paper.

2.2 The ENLSE based on FFT

In this section, the formulations of the ENLSEs will be presented. In the first subsection, the various forms of existing ENLSEs are outlined. The second subsection then explains the ENLSE based on FFT, newly proposed in this paper. Details are given below.

2.2.1   Existing ENLSEs

As the NLSE has been studied extensively, the basic equations are only given here for completeness without the details of derivation. The surface elevation and the velocity

potential could be written in the form of the summation of harmonics by introducing the concept of envelope

$$\eta = \bar{\eta} + \frac{1}{2}\left(Ae^{i\theta} + A_2 e^{2i\theta} + A_3 e^{3i\theta} + \cdots + c.c.\right) \tag{23}$$

$$\phi = \bar{\phi} + \frac{1}{2}\left[Be^{i\theta+z} + B_2 e^{2(i\theta+z)} + B_3 e^{3(i\theta+z)} + \cdots + c.c.\right] \tag{24}$$

where A and B are complex envelops of the first harmonic of surface elevation and velocity potential respectively, A_i and B_i are the ith harmonic coefficients, $\bar{\eta}$ and $\bar{\phi}$ are real functions representing the mean surface deflection and mean flow, $c.c.$ is the complex conjugate, and $\theta = X - T$ with X being the main direction of wave propagation. A, A_i and $\bar{\eta}$ have been non-dimensionalized by multiplying k_0, while B, B_i and $\bar{\phi}$ non-dimensionalized by multiplying $\sqrt{k_0^3/g}$, similar to what have been done for the variables in Eqs. (1)-(4). Subjected to the assumption that steepness $\varepsilon = k_0 a_0 \ll 1$ and spectrum width is of order $O(\varepsilon)$, one can introduce the slow modulation variables εX, εY, εZ and εT, and assume A and B are slowly modulated by such variables. Using the perturbation approach to the fourth order $O(\varepsilon^4)$, one can obtain the Dysthe equation [42, 45], which is in terms of B. One can also obtain the Dysthe equation of the second kind [68] in term of wave envelope A, which is employed in this paper:

$$\frac{\partial A}{\partial T} + \frac{1}{2}\frac{\partial A}{\partial X} + \frac{i}{8}\frac{\partial^2 A}{\partial X^2} + \frac{i}{4}\frac{\partial^2 A}{\partial Y^2} - \frac{1}{16}\frac{\partial^3 A}{\partial X^3} + \frac{3}{8}\frac{\partial^3 A}{\partial X \partial Y^2}$$
$$= -\frac{i}{2}|A|^2 A - \frac{3}{2}|A|^2\frac{\partial A}{\partial X} - \frac{A^2}{4}\frac{\partial A^*}{\partial X} - iA\frac{\partial \bar{\phi}}{\partial X} \tag{25}$$

$$\frac{\partial \bar{\phi}}{\partial Z} = \frac{1}{2}\frac{\partial |A|^2}{\partial X}, \quad Z = 0 \tag{26}$$

$$\Delta \bar{\phi} = 0, \quad Z \le 0 \tag{27}$$

$$\frac{\partial \bar{\phi}}{\partial Z} = 0, \quad Z = -\infty \tag{28}$$

where the superscript $*$ denotes its complex conjugate. The order (I) of the equation is defined in the way that

$$A^I \sim O(\varepsilon^I), \ \bar{\phi} \sim O(\varepsilon^2)$$

$$\frac{\partial}{\partial T} \sim O(\varepsilon), \ \frac{\partial}{\partial Z} \sim O(\varepsilon) \text{ and } \frac{\partial^I}{\partial X^I}, \frac{\partial^I}{\partial Y^I} \sim O(\varepsilon^I) \tag{29}$$

Trulsen et al. [44] later pointed out that the linear operators could be replaced by the exact linear solution, and proposed the following form

$$\frac{\partial A}{\partial T} + F^{-1}\{i(\omega - 1)F\{A\}\} = -\frac{i}{2}|A|^2 A - \frac{3}{2}|A|^2\frac{\partial A}{\partial X} - \frac{A^2}{4}\frac{\partial A^*}{\partial X} - iA\frac{\partial \bar{\phi}}{\partial X} \tag{30}$$

where $\omega = \sqrt{|k_0 + K|}$ and $k_0 = (1,0)$ is the peak wave number. Note that we have assumed that the mean wave direction points to the positive x-axis. The linear terms on the left hand side now become the exact representation of linear propagation and no longer subject to the narrow spectrum assumption. The nonlinear terms on the right hand remain the same. The method based on Eq. (30) is named as ENLSE-4 in this paper for convenience. The term $\bar{\phi}$ needs to be determined before the equations can be solved numerically, which is given by Eq. (A. 8) in Appendix-I. Substituting Eq. (A. 8) into Eq. (30), we have the other form of the ENLSE-4

$$\frac{\partial A}{\partial T} + F^{-1}\{i(\omega - 1)F\{A\}\} = \Psi_1 \tag{31}$$

where

$$\Psi_1 = Y_1 + \frac{i}{2}AF^{-1}\left\{\frac{\kappa^2}{K}F\{|A|^2\}\right\} \tag{32}$$

$$Y_1 = -\frac{i}{2}|A|^2A - \frac{3}{2}|A|^2\frac{\partial A}{\partial X} - \frac{1}{4}A^2\frac{\partial A^*}{\partial X} \tag{33}$$

and $F\{\}$ is the Fourier transform defined by Eq. (5) and (6). Eq.(31) is equivalent to the equation of first kind in terms of B derived by Clamond et al. [64], and is easy to be solved numerically if the initial condition $A(X, T = 0)$ is given.

Zakharov [38] had pointed out that the CNLSE could be derived from the Zakharov equation with narrow spectrum assumption. Later, Stiassinie [45] found that the Dysthe equation could also be derived from Zakharov equation by expanding the nonlinear terms to the specific order. Based on the same idea, Dabsarma and Das [46] made one step further and obtained the Higher Order Dysthe equation in terms of the Hilbert transform. Specifically, they gave the following equations

$$\frac{\partial A}{\partial T} + F^{-1}\{i(\omega - 1)F\{A\}\} = \Psi_2 \tag{34}$$

where the nonlinear part

$$\Psi_2 = Y_1 + Y_2 - \frac{i}{2}A\mathcal{H}\left\{\frac{\partial|A|^2}{\partial X}\right\} - \frac{1}{2}\frac{\partial A}{\partial X}\mathcal{H}\left\{\frac{\partial|A|^2}{\partial X}\right\} - \frac{1}{4}A\frac{\partial}{\partial X}\mathcal{H}\left\{A\frac{\partial A^*}{\partial X}\right\}$$
$$- \frac{1}{2}A\frac{\partial}{\partial X}\mathcal{H}\left\{A^*\frac{\partial A}{\partial X}\right\} + \frac{i}{8}A\frac{\partial^2}{\partial X^2}\mathcal{P}\left\{\frac{\partial|A|^2}{\partial X}\right\} \tag{35}$$
$$- \frac{1}{2}\frac{\partial A}{\partial Y}\mathcal{H}\left\{\frac{\partial|A|^2}{\partial Y}\right\} - \frac{1}{2}A\frac{\partial}{\partial Y}\mathcal{H}\left\{A^*\frac{\partial A}{\partial Y}\right\}$$

$$Y_2 = \frac{5i}{8}|A|^2\frac{\partial^2 A}{\partial X^2} + \frac{9i}{16}A^*\left(\frac{\partial A}{\partial X}\right)^2 + \frac{i}{8}A\frac{\partial A}{\partial X}\frac{\partial A^*}{\partial X} - \frac{i}{8}A^2\frac{\partial^2 A^*}{\partial X^2} + \frac{5i}{8}A^*\left(\frac{\partial A}{\partial Y}\right)^2$$
$$- \frac{i}{4}A\frac{\partial A}{\partial Y}\frac{\partial A^*}{\partial Y} - \frac{i}{4}A^2\frac{\partial^2 A^*}{\partial Y^2} \tag{36}$$

and the Hilbert transform is

$$\mathcal{H}\{A(\boldsymbol{X})\} = \frac{1}{2\pi} \int_{-\infty}^{\infty} A(\boldsymbol{X}') \frac{X' - X}{|\boldsymbol{X}' - \boldsymbol{X}|^3} d\boldsymbol{X}' \tag{37}$$

$$\mathcal{P}\{A(\boldsymbol{X})\} = \frac{1}{2\pi} \int_{-\infty}^{\infty} A(\boldsymbol{X}') \frac{X' - X}{|\boldsymbol{X}' - \boldsymbol{X}|^2} d\boldsymbol{X}' \tag{38}$$

For convenience, this formulation is named as ENLSE-5H.

2.2.2 The ENLSE-5F

In order to estimate the Hilbert transform, i.e., the Cauchy integral, involved in Ψ_2, numerical integration should be used. The difficulties with performing the numerical integration for these Cauchy integrals exist in two aspects. Firstly, the range of the integration is from $-\infty$ to ∞, although it could be optimized to a limited range, a large number of numerical tests may need to be carried out in order to determine this range and the tests may be needed for different cases as the range may depend on the specific value of envelope. Secondly, the integrals are weakly singular at $\boldsymbol{X}' = \boldsymbol{X}$ and so they require de-singular technique. Although the techniques can be developed, they need extra computational effort. In order to eliminate the difficulties, we suggest an equivalent formulation by introducing the following substitution (refer to Appendix-II)

$$F\{\mathcal{H}\{A(\boldsymbol{X})\}\} = \frac{i\kappa}{K} F\{A(\boldsymbol{X})\} \tag{39}$$

$$F\{\mathcal{P}\{A(\boldsymbol{X})\}\} = \frac{i\kappa}{K^2} F\{A(\boldsymbol{X})\} \tag{40}$$

Using the definitions, Eqs. (34) to (36) are then replaced by

$$\frac{\partial A}{\partial T} + F^{-1}\{i(\omega - 1)F\{A\}\} = \Psi_3 \tag{41}$$

where

$$\Psi_3 = \Upsilon_1 + \Upsilon_2 + \frac{i}{2} A F^{-1}\left\{\frac{\kappa^2}{K} F\{|A|^2\}\right\} + \frac{1}{2}\frac{\partial A}{\partial X} F^{-1}\left\{\frac{\kappa^2}{K} F\{|A|^2\}\right\}$$

$$+ \frac{1}{4} A F^{-1}\left\{\frac{\kappa^2}{K} F\left\{A\frac{\partial A^*}{\partial X}\right\}\right\} + \frac{1}{2} A F^{-1}\left\{\frac{\kappa^2}{K} F\left\{A^*\frac{\partial A}{\partial X}\right\}\right\}$$

$$+ \frac{i}{8} A F^{-1}\left\{\frac{\kappa^4}{K^2} F\{|A|^2\}\right\} + \frac{1}{2}\frac{\partial A}{\partial Y} F^{-1}\left\{\frac{\kappa\zeta}{K} F\{|A|^2\}\right\} \tag{42}$$

$$+ \frac{1}{2} A F^{-1}\left\{\frac{\kappa\zeta}{K} F\left\{A^*\frac{\partial A}{\partial Y}\right\}\right\}$$

12

The new form (Eq.(41) and (42)) is referred as the fifth order Enhanced Nonlinear Schrödinger Equation based on Fourier transform, shortened as ENLSE-5F.

Through comparing Ψ_2 and Ψ_3, it is found that the difference between the ENLSE-5H and ENLSE-5F is that the terms involving the Hilbert transform are now replaced with these in terms of the Fourier transform. The benefit by this substitution is that it is much easier to perform the Fourier transform than the Hilbert transform. In the ENLSE-5F, there are no difficulties described above associated with ENLSE-5H. Another benefit of using the ENLSE-5F is that it is also solved by FFT technique, same as for the ESBI and QSBI methods. If the ENLSE-5H would be coupled with them, extra FFT analysis must be performed after numerically estimating the Hilbert transform, which needs extra computational time. Nevertheless, it requires performing FFT twice for each corresponding term in Eq. (42), so that further investigations are needed in order to compare the computational efficiency with estimating Ψ_2 by using numerical integration. Furthermore, the periodical boundary condition needs to be imposed in the new formulation. However, following other studies on large scale random sea simulations [29, 31, 50, 65], the random sea states are usually reconstructed by assuming periodical boundary condition.

In addition, comparing the nonlinear part of the ENLSE-4, i.e., Eq. (32) with that of ENLSE-5F, i.e., (42), it is found that, apart from Υ_1 and $1/2AF^{-1}\{\kappa^2/KF\{|A|^2\}\}$, there are also Υ_2 and the rest parts in terms of the Fourier transform of order $O(\varepsilon^5)$ in Eq. (42). That means that the nonlinear effects in the ENLSE-5F are one order higher than the ENLSE-4.

3   Numerical techniques for coupling the ENLSE-5F, QSBI and ESBI

Table 1
Short summary of the three models

	ENLSE-5F	QSBI	ESBI
Efficiency	Super-fast. Most efficient among the three models.	Very fast. Efficiency between the ENLSE-5F and ESBI.	Fast. Least efficient among the three models
Accuracy	Accurate for small steepness and narrow spectrum waves. Least accurate among the three models	Accurate for small and mild steepness waves. Accuracy between the ENLSE-5F and ESBI	Accurate for small, mild and large steepness waves. Most accurate among the three models

Three methods (ESBI, QSBI and ENLSE-5F) described above are summarized in Table 1. The ESBI is the most accurate among the three as it is a fully nonlinear model without ignoring any necessary terms. Although QSBI only gives the solution of vertical velocity to the third order, the boundary conditions and governing equations remain to be fully nonlinear. There will not be significant difference between the ESBI and QSBI when the wave steepness is not high. The ENLSE-5F like other NLSE models is derived from simplified boundary conditions and subjected to limitations on both steepness and spectrum width. So the

13

ENLSE-5F is the least accurate model among all. On the other hand, the ENLSE-5F is the most efficient model. Due to the complexities in solving for the vertical velocity, the QSBI costs more computational efforts than the ENLSE-5F. Furthermore, the involvements of higher order nonlinear parts in solving for the vertical velocity make the ESBI less efficient than the QSBI. In terms of accuracy there is a relation: ESBI > QSBI > ENLSE-5F while ENLSE-5F > QSBI > ESBI in terms of efficiency, where '>' means superior. Based on this, a hybrid method will be formed using the three methods, which is both accurate and efficient, making use of the advantages of the three methods. For this purpose, the three methods (ESBI, QSBI and ENLSE-5F) should be alternatively and automatically employed according to the instantaneous wave information. That is, the simulation of the hybrid method will involve the switching from one model to another. To do so, the following challenges need to be tackled.

a) The conditions need to be found out to determine which model is employed during simulation and when switching to others. This will be discussed in Section 3.2.

b) To employ the three models alternatively, exchanging data from the ENLSE-5F to the QSBI and ESBI is necessary, i.e., the outputs of the ENLSE-5F need to be transformed to the forms accepted by the QSBI and ESBI as their input. The solution obtained from the ENLSE-5F at each time step is the free surface envelope A. To use them as the input for the QSBI and ESBI, the expressions for the free surface elevation and velocity potential in terms of A needs to be derived. This will be discussed in Subsection 3.1.1.

c) On the other hand, in order to exchange data from the QSBI and ESBI to the ENLSE-5F, their outputs need to be transformed to the forms of the input for the ENLSE-5F, which will be resolved in subsection 3.1.2.

3.1 Relationship between η and A

3.1.1 Transformation from A to η and ϕ

As can be seen from equations given in previous sections, the solution of the ENLSE-5F is given in terms of envelop A, but η and ϕ are required to start the QSBI or ESBI. Therefore, there is a need to transform A to η and ϕ when switching from the ENLSE-5F simulation to the QSBI or ESBI simulations. According to Eq. (23) and (24), we just need to estimate the harmonic coefficients A_2, A_3, B, B_2, B_3, and the term of $\bar{\eta}$. As shown in Appendix-III, they can be determined by using Eq.(A. 21), (A. 22), (A. 30), (A. 31), (A. 19) and (A. 24) respectively.

It is worth of noting that (A. 30) is different from Hogan's formulation [69], i.e., $B = -iA + 0.5\partial A/\partial X$, which only considers the approximate linear evolution of ϕ and nonlinear effects are neglected. In contrast, (A. 30) involves the nonlinear effects up to the third order. After all the harmonic coefficients above are evaluated, the surface elevation η and velocity potential ϕ are estimated by using Eq. (23) and (24).

3.1.2 Transformation from η to A

When switching the modelling from the QSBI or ESBI simulations to the ENLSE-5F simulations, one needs to obtain the expression for envelop A used for the input to the latter. That means that the spatial solution of the free surface elevation from the QSBI or ESBI needs to be transformed to the envelop A. In order to do so, we rewrite Eq.(23) as

$$\eta = \bar{\eta} + \eta_1 + \eta_2 + \eta_3 \tag{43}$$

where

$$\eta_1 = \frac{1}{2}\left(Ae^{i\theta} + c.c.\right), \quad \eta_2 = \frac{1}{2}\left(A_2 e^{2i\theta} + c.c.\right)$$

$$and \quad \eta_3 = \frac{1}{2}\left(A_3 e^{3i\theta} + c.c.\right) \tag{44}$$

are the 1st, 2nd and 3rd harmonics of the free surface elevation, respectively. The relationship between A and η_1 is established by using (A. 38) in Appendix-IV. In addition, η_2, η_3 and $\bar{\eta}$ could be estimated with the help of Eq.(A. 21), (A. 22) and (A. 24). However, it is the value of η that is given from the solution of the QSBI or ESBI instead of η_1, η_2, η_3 and $\bar{\eta}$. To overcome this dilemma, iterations are carried out for obtaining the solution A from η, which is graphically illustrated in Fig. 1. It is noted that η and η_1 are in the same order, which are normally much larger than η_2, η_3 and $\bar{\eta}$, and so the iterative procedure starts from $\eta_1 = \eta$.
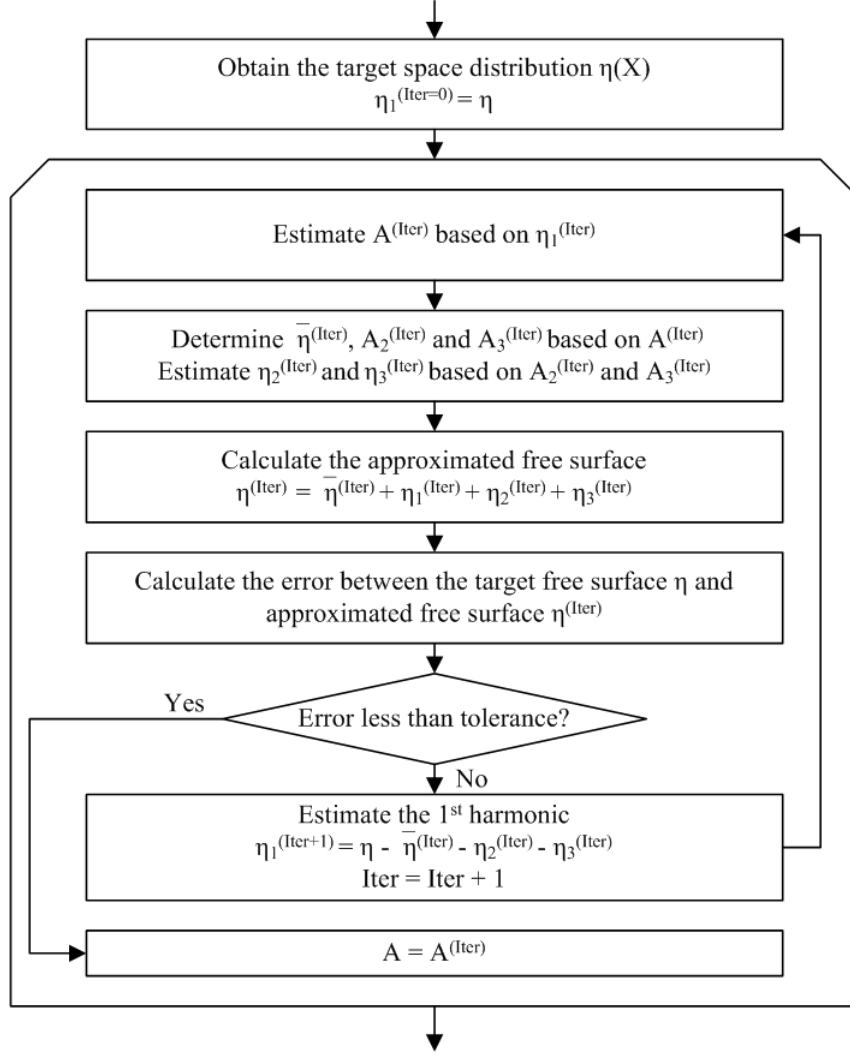
Fig. 1. Flow chart of estimating the envelope A by iterations

The error represents the difference between the target surface η and the approximated surface $\eta^{(Iter)}$ is given as

$$Err_A = \frac{\int |\eta - \eta^{(Iter)}| dX}{\int |\eta| dX} < Tol_A \tag{45}$$

We have found that $Tol_A = 10^{-5}$ is enough to give very precise results.

3.2 Methodology for combining three methods

In order to form a hybrid method, the three methods — ENLSE-5F, QSBI and ESBI need to be combined together. To do so, the key thing is the conditions under which the simulation is switched from one to another. For this purpose, we introduce four conditions:

a) Condition 1: $Err_1 > Tol_1$, $|\eta(T)|_{max} > |\eta(T = 0)|_{max}$ and
$|\eta(T)|_{max} > |\eta(T - \Delta T)|_{max}$

b) Condition 2: $Err_1 \leq Tol_1$, $|\eta(T)|_{max} \leq |\eta(T = 0)|_{max}$ and

16

$$|\eta(T)|_{max} \leq |\eta(T - \Delta T)|_{max}$$

    c)   Condition 3: $Err_2 > Tol_2$

    d)   Condition 4: $Err_2 \leq Tol_2$

where

$$Err_1 = \frac{\max\{|\Psi_3 - \Psi_1|\}}{\max\{|A|\}} \tag{46}$$

$$Err_2 = \frac{\max\left|V_3^{(1)}\right|}{\max|V|} \tag{47}$$

The basic idea of the four conditions aforementioned is to measure the intensity of the nonlinearities, i.e., the stronger the waves are, the larger Err_1 and Err_2 are. The first two conditions are used to control the switch between the ENLSE-5F and QSBI. If the waves keep growing, and finally the steepness is larger than the initial steepness and $Err_1 > Tol_1$, Condition 1 is met and the waves are no longer weakly nonlinear, which means actions should be taken to replace the ENLSE-5F by using the QSBI. Vice versa, if Condition 2 is met, the ENLSE-5F will be recovered. Similarly, the last two conditions are used to control the switch between the QSBI and ESBI. If $Err_2 > Tol_2$, the nonlinearities become so strong that the QSBI should be replaced with the ESBI, and vice versa.

With the four conditions and the formulas for the errors above, the flow chart for the hybrid method is given in Fig. 2. It shows that the procedure starts with ENLSE-5F for waves with small steepness; when Condition 1 is met (the wave being steep enough), FLAG will be assigned to be 2 and so the process will be switched to QSBI in the next time step; after the waves become steeper and so Condition 3 is met, the process will be switched to ESBI in the next time step. During the simulation, if the waves become less steep (or Condition 4 is met), FLAG will be assigned to be 2 from the ESBI and so the process will be switched back to QSBI, then may be to ENLSE-5F if Condition 2 is met. As can be understood, the switch is always through QSBI and there is no direct switch between the ENLSE-5F and the ESBI. It is noted that the process can start from any one of the three methods, as long as the initial value of FLAG is assigned properly. For example, if one knows that the wave spectrum is not narrow-banded and/or the wave steepness is quite large, the initial value of FLAG may be given as 3 and so the process will start from ESBI. Of course, the representation of the initial condition will be different if the starting method is different. Actually, the initial condition is usually given in terms of the free surface elevation and the velocity potential on the free surface as shown in [63], which can be employed directly to start QSBI or ESBI. For start with ENLSE-5F, the initial condition information in terms of the free surface elevation and the velocity potential needs to be transformed to the wave envelope in the similar way to that discussed in Section 3.1.2.
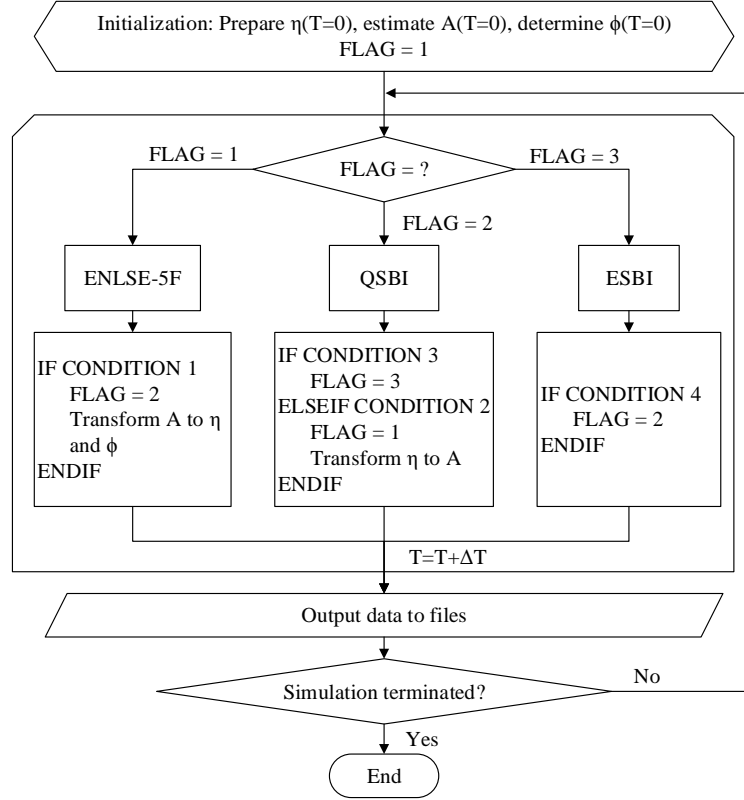
Fig. 2. Flow chart for the new hybrid method

3.3 Effects of Tol_1 and Tol_2 by numerical simulations

In order to control the switch between the three models and guarantee the final results are acceptable, proper values for Tol_1 and Tol_2 need to be specified. Thus in this section we will discuss how the values for Tol_1 and Tol_2 are determined. For this purpose, numerical simulations of random waves in a two-dimensional domain of $128L_0$ and duration of $1000T_0$ will be performed by using the ENLSE-5F, QSBI and ESBI separately.

Two most frequently used spectra, JONSWAP and Wallops, will be considered. As well known, the JONSWAP spectrum is proposed for developing sea states while the Wallops spectrum is more suitable for fully developed and decaying sea states [70]. The JONSWAP spectrum in terms of the wave number in dimensionless form is given as [28]

$$S_J(k) = \frac{\alpha_J H_s^2}{2k^3} \exp\left[-\frac{5}{4}\left(\frac{1}{k}\right)^2\right] \gamma^{\exp\left[-(\sqrt{k}-1)^2/(2\sigma^2)\right]} \tag{48}$$

where the wave number k has been non-dimensionalized by dividing the peak wave number k_0, the significant wave height H_s by multiplying k_0, $S_J(k)$ by multiplying k_0^5,

$\alpha_J = 0.0624(1.094 - 0.01915 ln\gamma)/[0.23 + 0.0336\gamma - 0.185(1.9 + \gamma)^{-1}]$, $\gamma \in [1,9]$ is

the peak enhancement factor and $\sigma = 0.07\,(k < 1)$ or $= 0.09(\,k \geq 1)$. The peak enhancement factor γ controls the width of the spectrum, and the larger γ is, the narrower

the spectrum is.

Meanwhile, the Wallops spectrum is reformulated by Goda [71] and its dimensionless form is

$$S_W(k) = \frac{\alpha_W H_s^2}{2k^{(m+1)/2}} exp\left[-\frac{m}{4k^2}\right] \tag{49}$$

where $\alpha_W = 0.06238 m^{(m-1)/4}[1 + 0.7458(m+2)^{-1.057}]/(4^{(m-5)/4}\Gamma[(m-1)/4])$ and $m \in [5,25]$ is the width parameter. The spectrum becomes narrower when m increases.

Different combinations of the significant wave height and width parameter are tested based on both the JONSWAP and Wallops spectrum, in order to find proper resolution and tolerance for time marching. The domain covers 128 peak wave lengths and is resolved into 8192 points. The spectrum is discretized by using interval $\Delta k = 2\pi/L_x$ (L_x is the domain length), and the cut-off wave number $k_{max} = 8$. According to Goda [71], a cut-off frequency chosen as the 1.5 to 2.0 times the peak frequency, is enough for engineering purpose, which is equivalent to the cut-off wave number $k_{max} = 2.25 \sim 4.0$, and is covered by that we have suggested. The errors of wave elevations will be estimated by

$$Err_\eta = \frac{\int |\eta - \eta_0| d\mathbf{X}}{\int |\eta_0| d\mathbf{X}} \tag{50}$$

where η is obtained by using a specific numerical model, and η_0 is the reference solution of wave elevations, which may be analytical solution or evaluated by using a relatively more accurate method.

3.3.1   Investigation on effects of Tol_2

Firstly, we carry out numerical simulations based on both JONSWAP and Wallops spectrum with different significant wave heights and spectrum width parameters spanning in the practical range in order to find a proper value for Tol_2. Because this parameter only controls the switch between the QSBI and the ESBI, $FLAG = 2$ and $Tol_1 = 0$ are given during the initialization in the process described in Fig. 2 in all the cases for testing effects of Tol_2.

The simulations are carried out to $1000T_0$ in a two-dimensional domain of $128L_0$ for random waves. The errors in the wave elevation are estimated by Eq. (50), in which η_0 is the free surface at the end of the simulation obtained by only using the ESBI model and η is that obtained by using the hybrid model with different values of Tol_2 specified. Some results are presented in Fig. 3, in which only the cases of narrowest and widest bandwidth are shown. From this figure, one can see that the trend of the error in wave elevations is very similar for the cases with different spectra, different significant wave heights and spectrum widths. It is also seen that for a fixed H_s and spectrum width, the error grows when Tol_2 increases. This is because that the larger value of Tol_2 allows more involvement of the QSBI during the simulation even when the QSBI is not quite accurate at some instance.

According to tests by Wang and Ma [63], the wave elevations become invisibly different if their error estimated by Eq. (50) is less than 5%. Based on this and also other tests when preparing this paper, $Err_\eta < 5\%$ is acceptable. Nevertheless, to be conserved and considering that the ENLSE-5F has not been involved yet, we may accept the error (Err_η) of the hybrid model to be not larger than 3% from the point of view of accuracy. On the other hand, we also hope that the value of Tol_2 is as large as possible. That is because the larger the value of Tol_2 is, the longer the QSBI is involved and so more computational time it saves. By examining all the curves in Fig. 3, one may find that the hybrid model with

$Tol_2 \leq 0.03\%$ leads to the error (Err_η) of less than 3% in all the cases with with different

spectra, different significant wave heights and spectrum widths. Therefore, generally, $Tol_2 = 0.03\%$ will be adopted for controlling the switch between QSBI and ESBI.

(a)

(b)

(c)

(d)
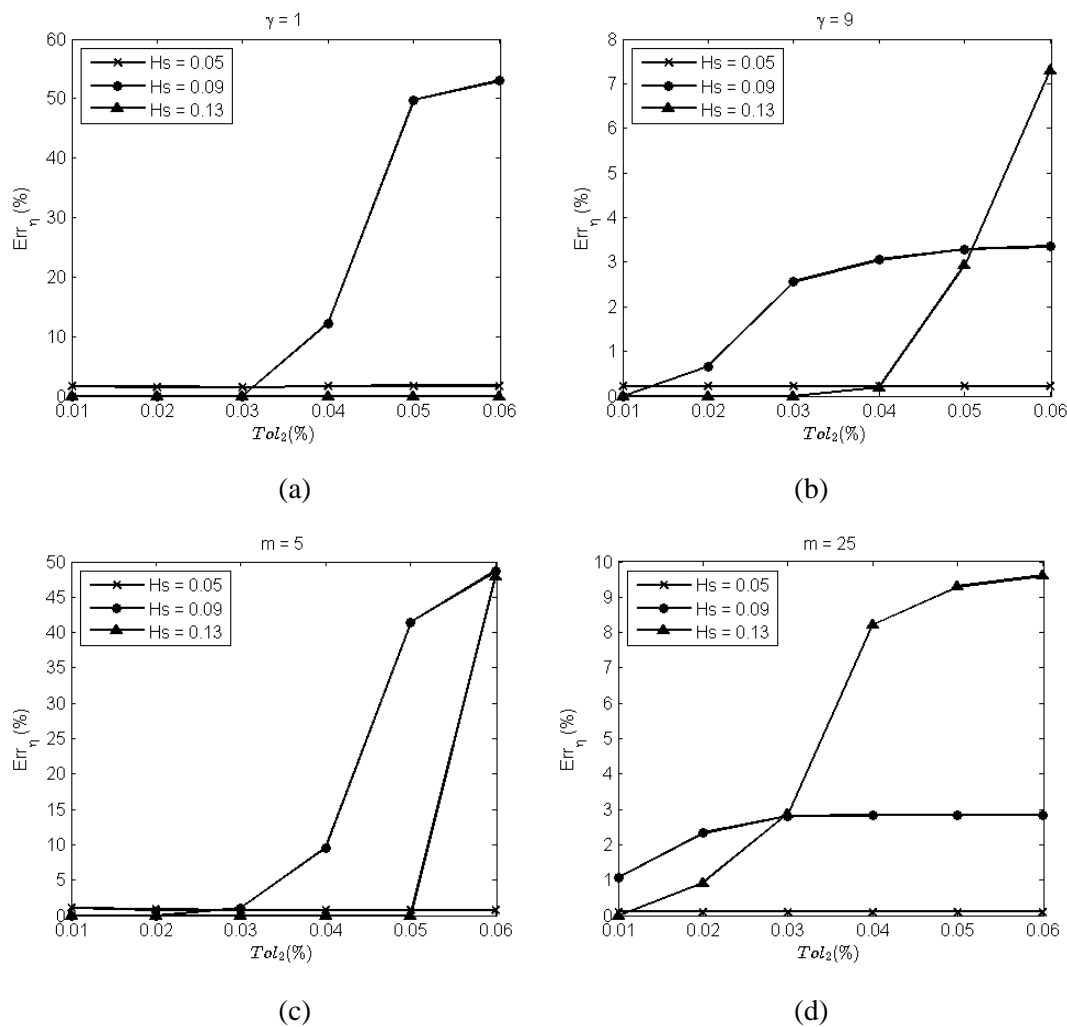
Fig. 3. Err_η against Tol_2. (a)(b) are based on JONSWAP spectrum and (c)(d) on Wallops spectrum

3.3.2   Investigation on effects of Tol_1

By using $Tol_2 = 0.03\%$, the numerical tests are carried out for the same cases again in order to find the appropriate tolerance of Tol_1 to control the switch between the ENLSE-5F and the QSBI. In these tests, all three models are involved in calculating the cases with different values of Tol_1 specified.

The results for the error (Err_η) are shown in Fig. 4. Again, it is found that the trend of the error in wave elevations is very similar for the cases with different parameters, and that for a fixed H_s and spectrum width, the error grows when Tol_1 increases.

As all three models are involved in these tests, $Err_\eta < 5\%$ may be considered to be acceptable in terms of accuracy and efficiency. By examining Fig. 4, one may find that the condition of $Err_\eta < 5\%$ can be satisfied if $Tol_1 = 0.02\%$ for all the cases. Therefore, 0.02% for Tol_1 can be used for controlling the exchange between the ENLSE-5F and QSBI.

(a)   (b)

(c)   (d)
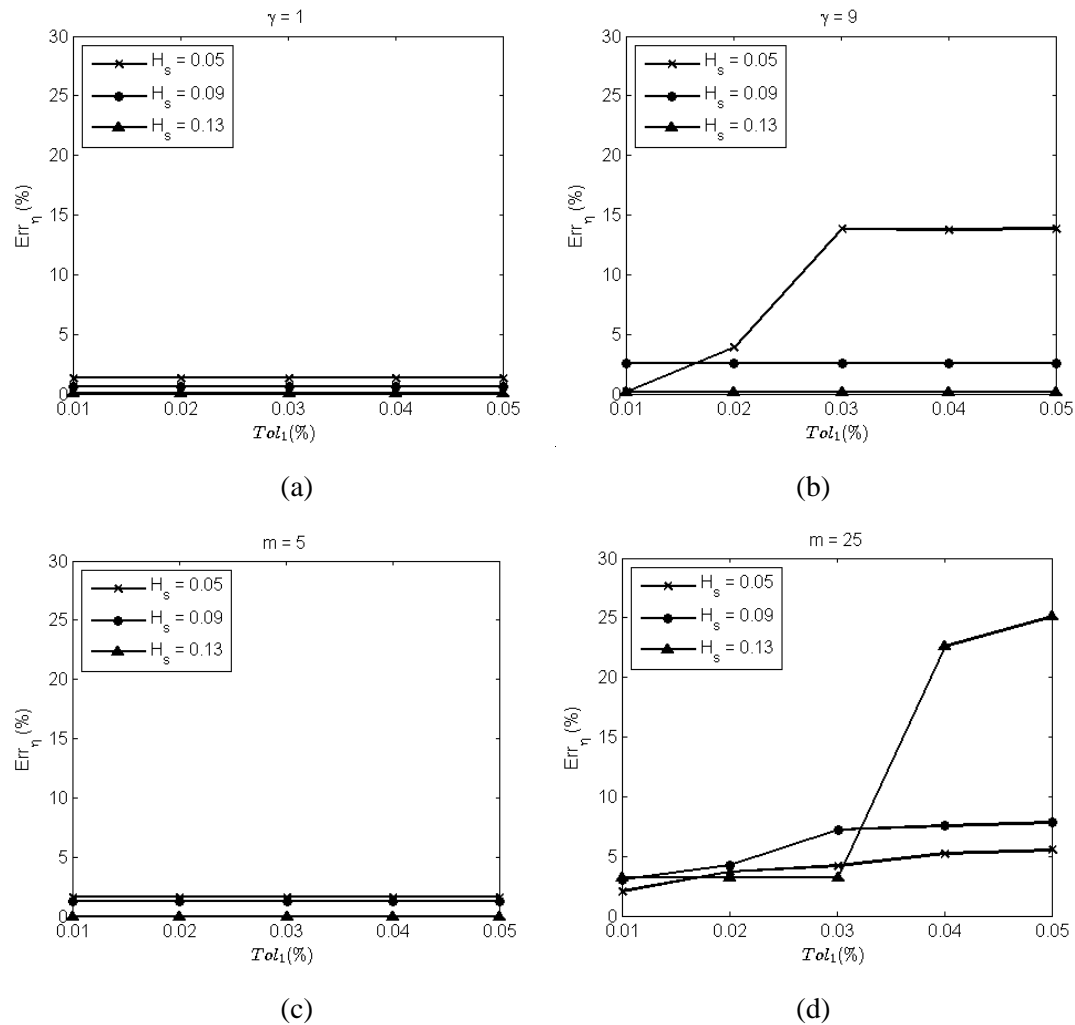
Fig. 4. Err_η against Tol_1. (a)(b) are based on JONSWAP spectrum and (c)(d) on Wallops

spectrum

It is worth of noting that the tolerance $Tol_1 = 0.02\%$ and $Tol_2 = 0.03\%$ are obtained based on large numbers of two dimensional (2D) simulations. However, it can be applied to three dimensional (3D) simulations as Eq. (46) and (47) can still be used. Next, numerical tests will be carried out to validate the hybrid model for both 2D and 3D simulations by using the tolerances obtained in this section for switching between models.

3.4 Validation

In order to validate the present model for larger domain and longer simulations, we compare the results of the hybrid model with the results in [64]. The free surfaces at several time steps obtained by this hybrid method and that in [64] are shown in Fig. 5. The difference between them is almost invisible, with its value at the maximum free surface being about 3.02% occurring at the end of the simulation. The comparison again indicates that the profiles by using the present method and the fully nonlinear method described in [64] are consistent. In addition, the switch between the models is shown in Fig. 6. It is found that after the first extreme wave event, the maximum free surface elevation never drops below the initial status, so that the ENLSE-5F is not involved again in the simulation after the first 100 periods. The rest of the simulation is completed by the switch between the QSBI and ESBI models. Nevertheless, the about 40% CPU time is saved in this case compared to that using the ESBI model alone.
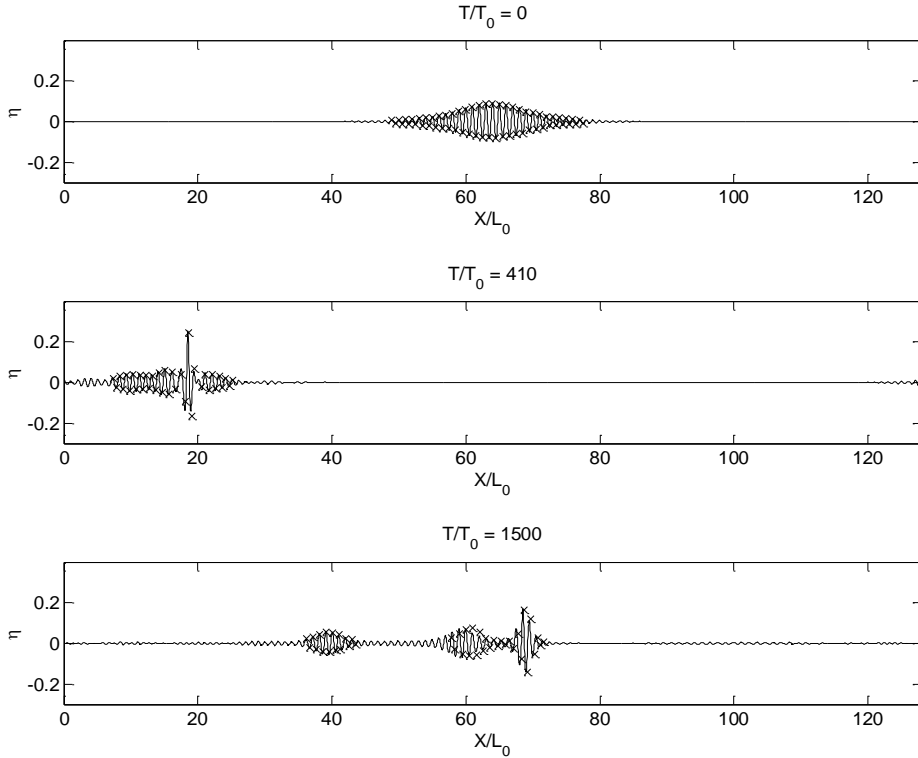
Fig. 5. Free surface at different instant. '—': Hybrid method; 'x' Method in [64]
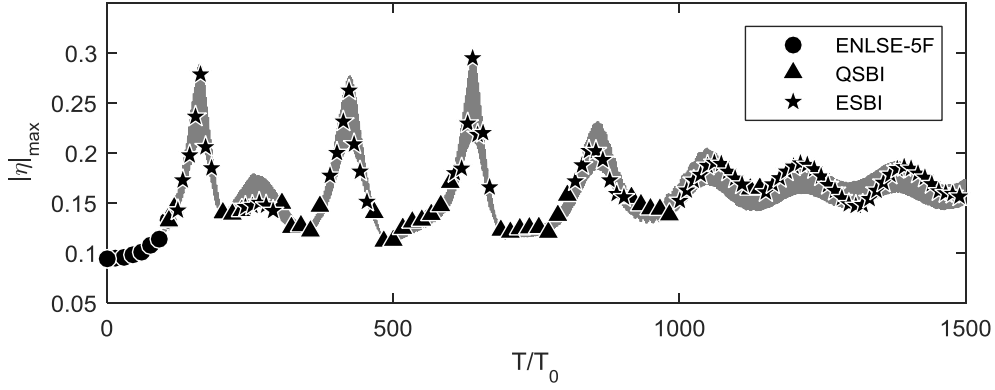
Fig. 6. The exchange between the models. Solid line represents the values of $|\eta|_{max}$

Moreover, in order to validate the hybrid model for three dimensional (3D) problems, the numerical tests for directional focusing wave described by Bateman et al. [72] is repeated here with the same setups. A focusing wave of steepness $\varepsilon = 0.3602$ as in [73] is generated at the center of the domain, and the profiles of the free surface along $Y/L_0 = 0$ at the focusing time for both the hybrid model and results in [72] are shown in Fig. 7. The error of the maximum surface elevation is about 2.02%, which means that the hybrid model successfully captured the occurrence of the focusing wave in the 3D case.

In order to show the effectiveness of the numerical technique for controlling the switch between models, the maximum free surface elevation against time is shown in Fig. 8 with indicators of each model used at that instant. It is found that the ENLSE-5F is only involved in the first 1.5 peak periods, while the majority of the simulation is run by QSBI and ESBI. However, it shows that the hybrid model successfully switched from the ENLSE-5F, to QSBI and then ESBI, when the maximum surface becomes larger and larger. This case with the parameters in Section 3.3 demonstrates that the hybrid model is also suitable for 3D wave problems.
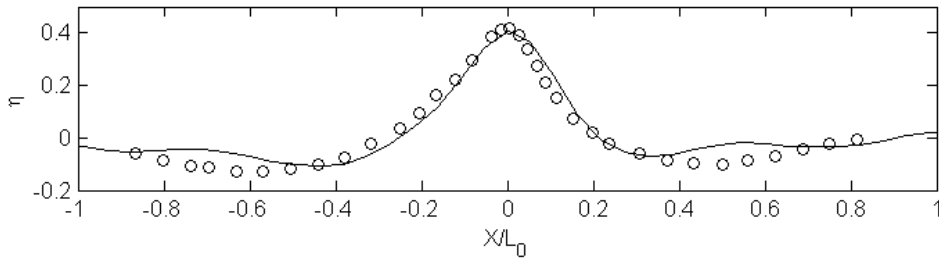
Fig. 7. The Profiles of free surface at $T/T_0 = 7.4$. '——': Hybrid model; 'o': Fully nonlinear model in [72]
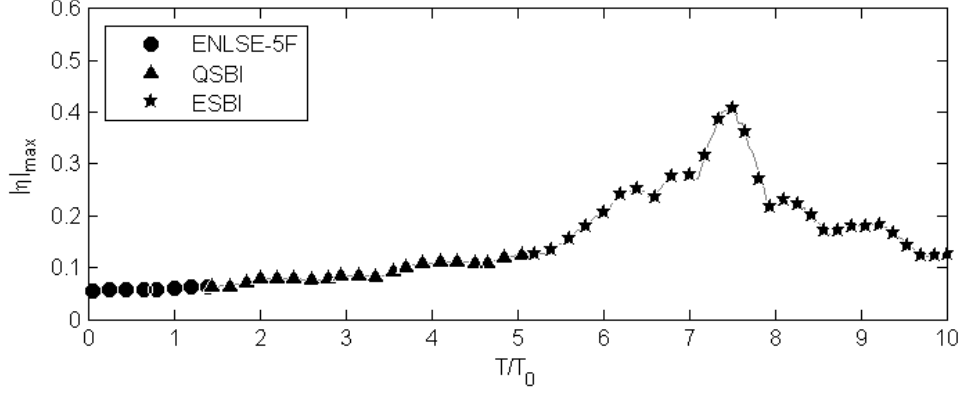
Fig. 8. The exchange between the models (solid line represents the values of $|\eta|_{max}$)

In addition, a simulation of the crescent wave pattern is also carried out in order to further validate the hybrid model for 3D cases. The test by Fructus et al. [74] is repeated here with the same setups. The following quantity is introduced to measure the ratio of the amplitude of component K' over the initial Stokes wave amplitude.

$$\Psi_\epsilon(K') = \frac{|F\{\eta\}|_{(K',T)}}{|F\{\eta\}|_{(K=(1,0),T=0)}} \tag{51}$$

The results are presented in Fig. 9 for the components of peak wave component $K' = (1,0)$ and perturbation component $K' = (1.5, 1.645)$. It shows that the results obtained by using the hybrid model is highly correlated with that obtained by using the method in [74] in this 3D case, which again confirms that the tolerance values obtained by using the 2D cases are suitable for the 3D cases. Similar to Fig. 6, the switch between the models is shown in Fig. 10, where it is found that the ENLSE-5F is not involved and only the QSBI and ESBI are used during the simulation for this case. And it shows that the hybrid model successfully switched from the QSBI to ESBI when the maximum wave steepness became large, which further confirms that the hybrid model can be used for simulating waves in three dimensions.
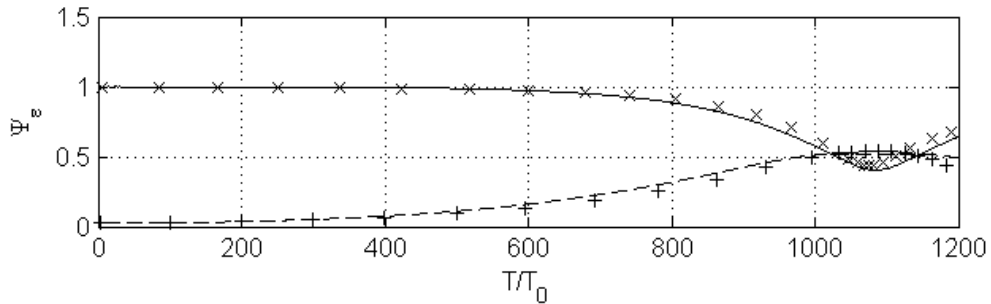
Fig. 9. Evolution of perturbation components and peak wave components: '—' $K' = (1,0)$ by using hybrid model; '--' $K' = (1.5, 1.645)$ by using hybrid model; 'x' $K' = (1,0)$ by using method in [74]; '+' $K' = (1.5, 1.645)$ by using method in [74]
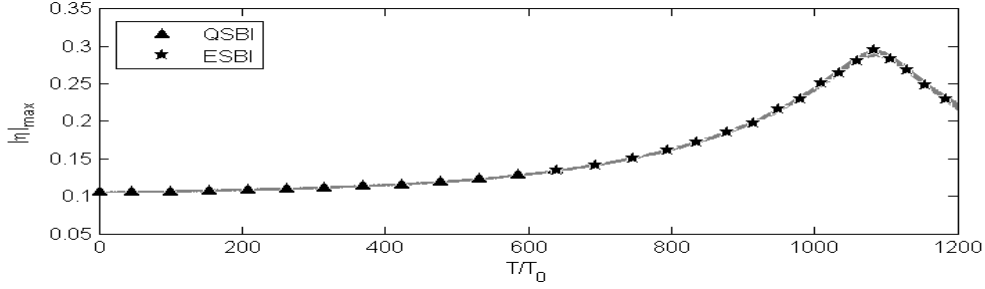
Fig. 10. The exchange between the models (solid line represents the values of $|\eta|_{max}$)

4   Discussions on the overall performance of the hybrid model

In this section, more numerical examples will be tested on the new hybrid model with $Tol_1 = 0.02\%$ and $Tol_2 = 0.03\%$, which are determined in Section 3.3.

We introduce the CPU time ratio that is the CPU time of the ESBI divided by that of the hybrid model. All the simulations are implemented by using a single core on the same workstation equipped with the Intel Xeon E5-2630 v2 (Intel Corporation, Santa Clara, CA, USA) of 2.6GHz processor. Pre-tests have been carried out based on the JONSWAP spectrum with $H_s = 0.13$, $\gamma = 5$, and it takes the ESBI 10638s ~ 3h, the QSBI 5404s ~ 1.5h (about a half of CPU time for the ESBI), and the ENLSE-5F only 734s ~ 12min (only 7% of CPU time for the ESBI), to finish one sea state simulation ($1000T_0$) covering a two dimensional domain of $128L_0$ domain by a resolution of 2^6 per L_0 independently.

Although the main purpose to develop the efficient hybrid method is for simulating the evolution of random seas with rogues wave occurrence, our simulations in this section will be mainly focused on the cases with tailored rogue waves embedded in random background for testing the performance of the new hybrid method and its applicability in various scenarios. That is because real rogue waves are unpredictable and could happen at arbitrary time and location, and so directly testing on them may not be able to check the performance of the new hybrid in various scenarios. The technique of embedding rogues waves in random background is commonly used in experiments. Different methods for embedding rogue waves in random background are suggested in literature. In order to constrain the occurrence of a rogue wave in a limited space during a predictable timeframe, Taylor, et al. [73] proposed a Constrained NewWave theory. Clauss and Steinhagen [75] has adopted a Sequential Quadratic Programming method to optimize the location and time instance of the maximum crest in space and time domain respectively so that an expected asymmetric wave profile is created. Kim [76] suggested a method to deform the largest crest wave by time and crest distortions in order to produce an asymmetric profile of the free surface. Their methods directly adjust the wave profiles through iterations until the criterions for rogue waves are satisfied. Furthermore, Kriebel and Alsina [77] proposed a different method to generate rogue waves in random sea by dividing the spectrum into two parts, one of which produces the rogue waves by superposition based on linear dispersion relation and the other forms the random background. Wang, et al. [78] have improved this method, which will be adopted in this study. The details are omitted for simplicity but could be found in [78].

4.1 Different rogue waves heights

Next, we keep the significant wave height unchanged, i.e., $H_s = 0.05$, and test on different rogue wave heights, i.e., $2H_s$, $3H_s$ and $4H_s$. The basic set-ups are the same with that for Fig. 3 and Fig. 4. Similar to these in the previous section, the errors of the free surface together with the CPU ratios are presented in Fig. 11 for the cases with different spectrum and different parameters.
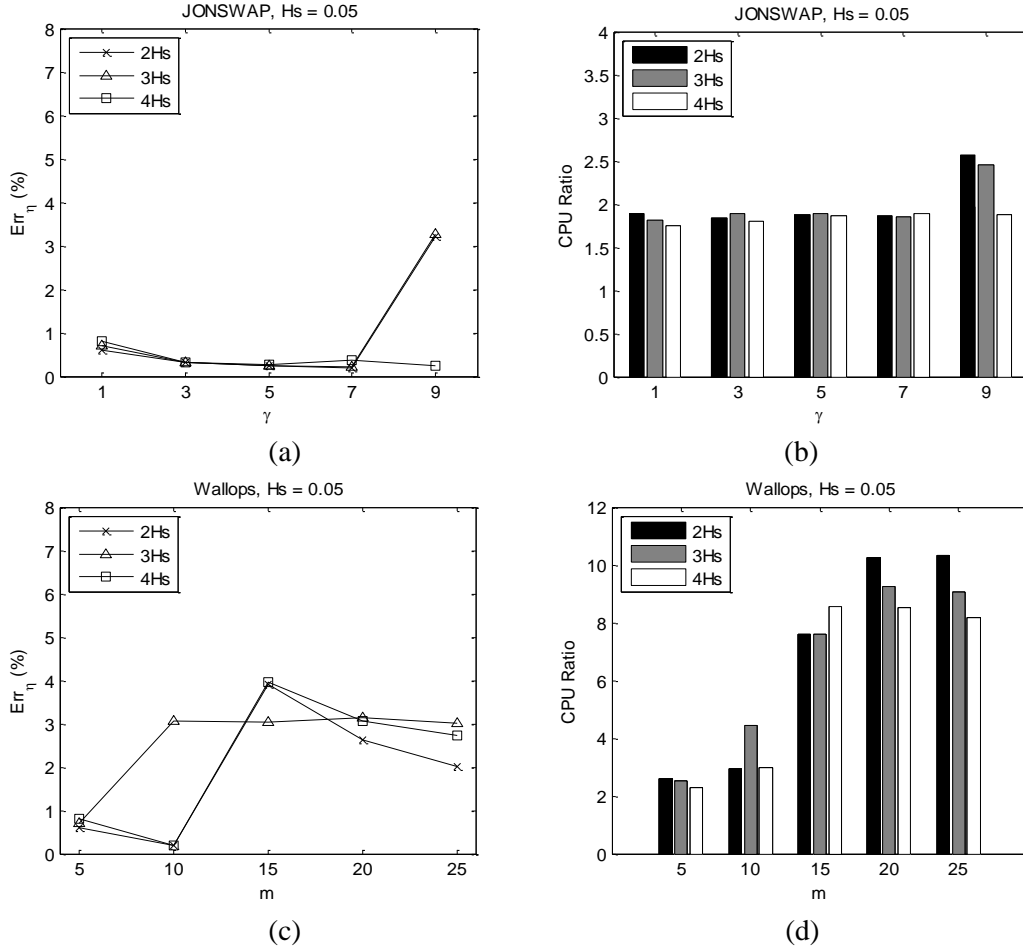

(a)   (b)

(c)   (d)

Fig. 11. Err_η and CPU ratio (CPU time of ESBI/CPU time of hybrid model) for the cases with different rogue wave heights

It shows that the errors in the cases for both the JONSWAP and Wallops spectra with different width parameters are less than 5%, which confirms that the values for the Tol_1 and Tol_2 controlling the switch between the models are appropriate for the cases with different embedded rogue waves. It can be seen from Fig. 11(b) that the CPU time ratio is approximately 1.9 in all cases with the JONSWAP spectrum, except for the cases with $2H_s \sim 3H_s$ and $\gamma = 9$. That is because the ENLSE-5F is involved only in these cases. When the ENLSE-5F is not involved, the calculation is switched only between the QSBI and ESBI models. As indicated above, the QSBI use about a half of CPU time used by ESBI, which implies that the QSBI are implemented in most of time steps for the cases except for these with $2H_s \sim 3H_s$ and $\gamma = 9$.

On the other hand, for the simulations based on the Wallops spectrum, the story is different in particular when $m > 10$. In these cases, the CPU time ratio is more than 8 or even 10, Fig. 11 (d), implying that the new hybrid method is very much more efficient than the ESBI only. When $m \leq 10$, the ratio is not so high, though it is still larger than 2.

In order to illustrate how the models switch during the simulation, Fig. 12 is presented in a similar way to that for Fig. 6. It shows that in some case, the process starts with ENLSE-5F, then goes to QSBI and ESBI, ending with QSBI, e.g, Fig. 12 (a). In some other cases, the process starts with ENLSE-5F, then goes to QSBI and ESBI, ending with ENLSE-5F, e.g, Fig. 12(d). The various scenarios illustrated in Fig. 12 demonstrate that the automatic switch between the three models works well.

Furthermore, the profiles with the rogue wave height of $4H_s$ at focusing time and location are shown in Fig. 13. It is found that the results obtained by using the hybrid model are almost identical with that obtained by using the ESBI only. However, the hybrid model significantly save the CPU time with different degrees as indicated above.

(a): $2H_s$

(b): $4H_s$

(c): $2H_s$

(d): $4H_s$
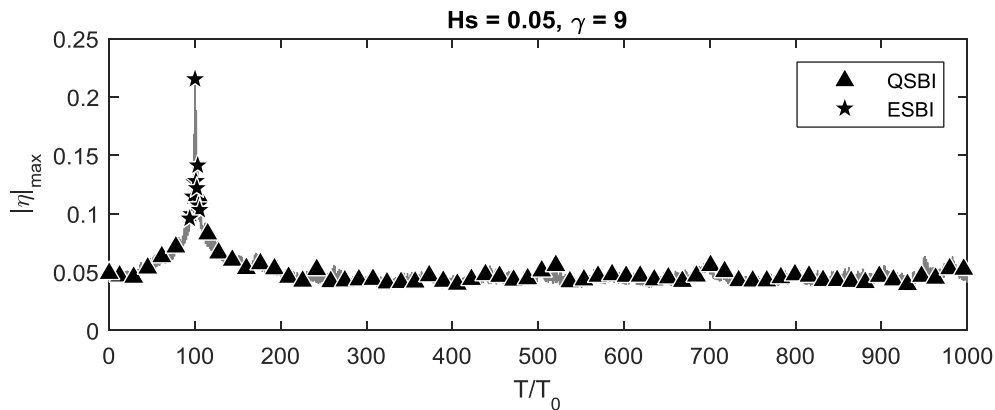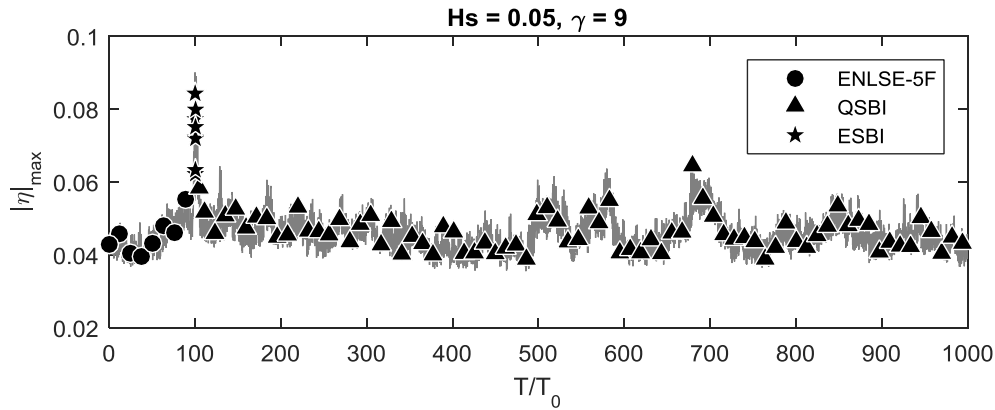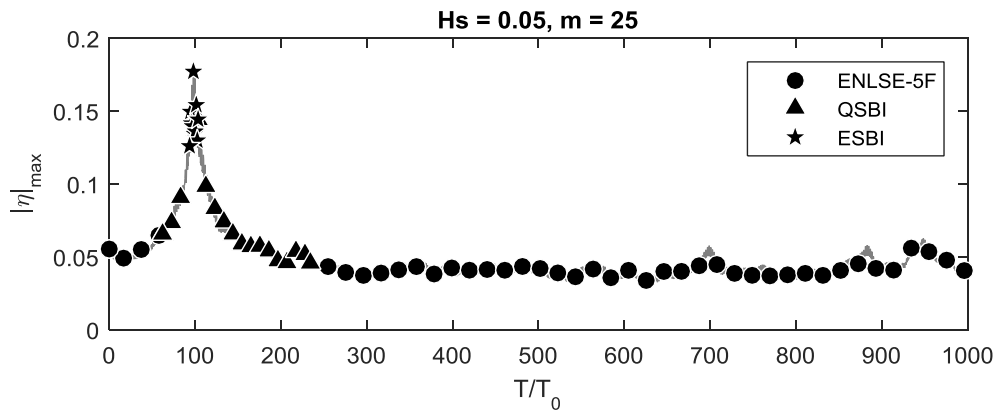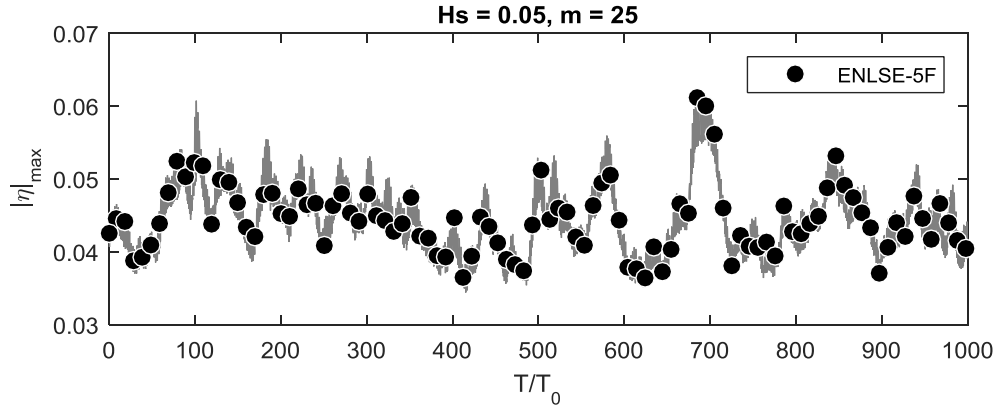
Fig. 12. Maximum wave elevations with indicators for which model is used for the cases with different rogue wave heights
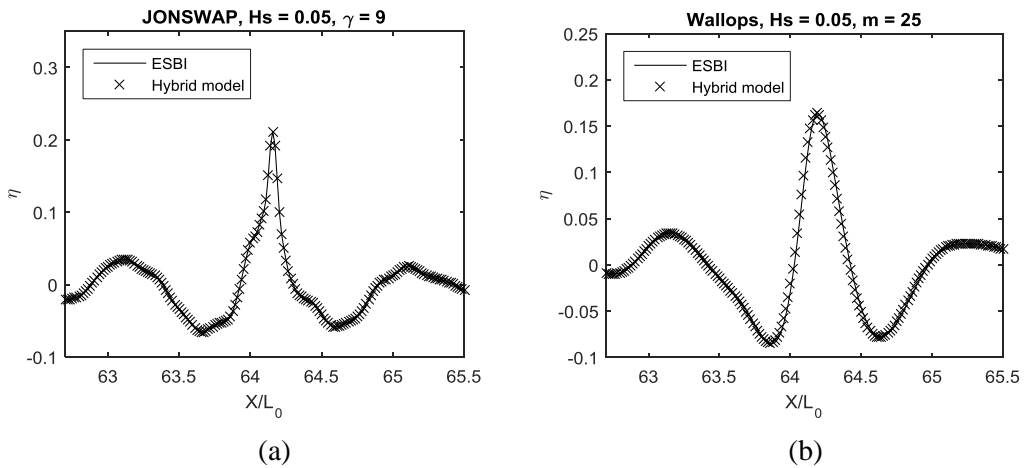

(a)

(b)

Fig. 13. The profiles of the rogue wave with height of $4H_s$ for the cases with different rogue wave heights

4.2 Different numbers of rogue waves in time domain

There are possibilities that more than one rogue wave events happen during one sea state

[9] at different times. Therefore, cases with different numbers of rogue wave events in a tie domain are investigated in this section. In addition to one rogue wave event $T_f/T_0 = 100$, the cases with two rogue wave events at $T_f/T_0 = 100 \ \& \ 500$ and three rogue wave events $T_f/T_0 = 100\&500\&900$ are studied by using the same set-ups with that for Fig. 3 and Fig. 4. The rogue wave height is fixed to $3H_s$ as there will not be energy left to generate the random background if three successive rogue waves higher than $3H_s$ are generated by using the method explained in [78]. Similarly, the errors and CPU time ratios are presented in Fig. 14.
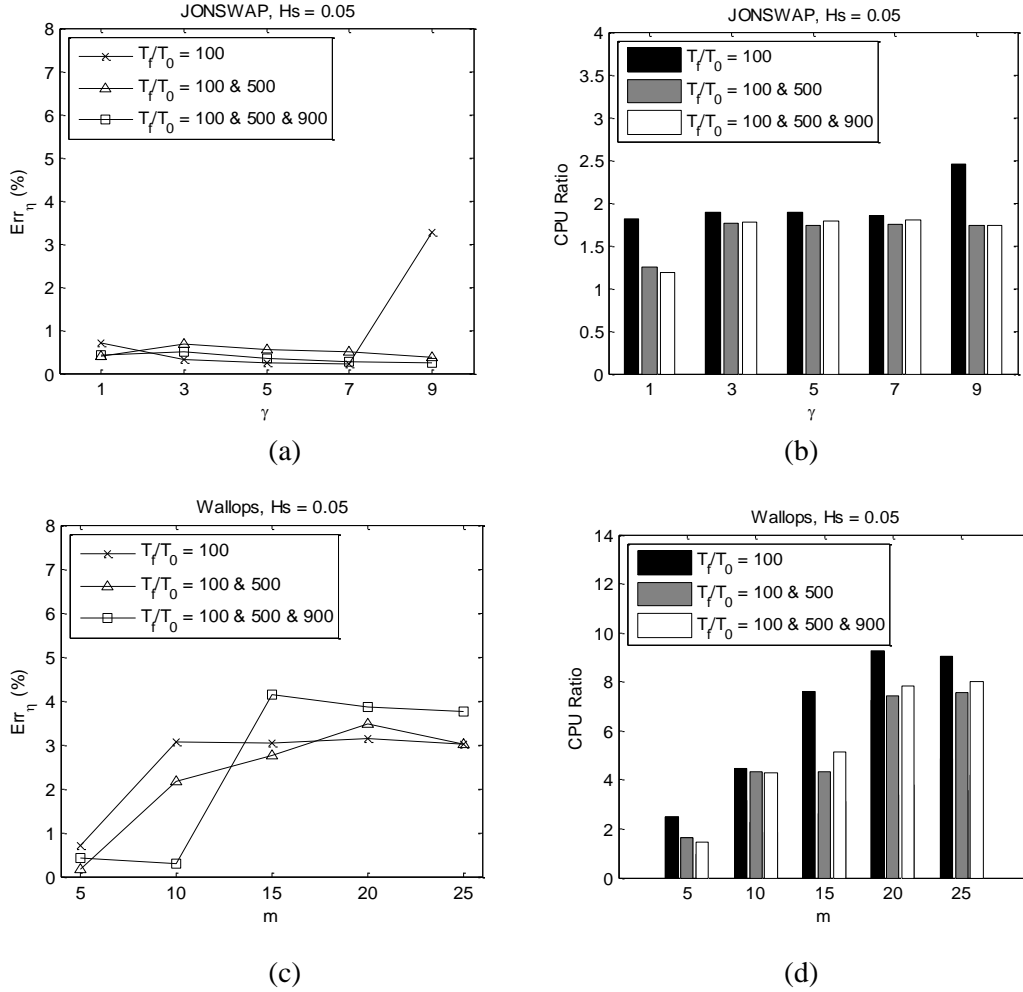
Fig. 14. Err_η and CPU ratio (CPU time of ESBI/CPU time of hybrid model) for the cases of different amount of rogue waves on temporal scale

As shown in Fig. 14 (a) and (c), the errors for all the cases considered in this section are less than 5%, which again confirms effectiveness of the values of Tol_1 and Tol_2 for controlling the switching in the cases with different amount of rogue waves on temporal scale.

It is shown in Fig. 14(b) that for the simulations based on the JONSWAP spectrum, the maximum CPU time ratio appears to be 2.5 for the case $T_f/T_0 = 100$ with $\gamma = 9$, and the ratio is about 2 in most other cases, which is largely similar to what has been observed in Fig. 11. The explanation there also applies to this figure. Besides, another two cases of

29

$T_f/T_0 = 100\&500$ and $T_f/T_0 = 100\&500\&900$ with $\gamma = 1$ are simulated mostly by the ESBI, so that the CPU time ratio is approximately 1.2, but a little higher than 1 due to the involvement of the QSBI and ENLSE-5F.

For the simulations based on the Wallops spectrum, the CPU time ratios are all larger than 4 except for the cases with $m = 5$, which are however approximately 2. Roughly speaking, the CPU time ratio increases when the spectrum becomes narrower (m increases). Among all the cases, the most efficient case is the one that rogue wave only occurs once at

$T_f/T_0 = 100$ with $m = 20$, which leads to the CPU ratio of 9.2.

In addition, in order to examine how the hybrid model switching between each model for the numerical examples in this section, similar graphs with Fig. 6 are presented in Fig. 15. It shows that for the cases based on the JONSWAP spectrum, the hybrid model can effectively switch from QSBI to ESBI, and then back to QSBI during each occurrence of rogue wave, e.g., Fig. 15(a)(b). For these based on the Wallops spectrum, the hybrid model starts with ENLSE-5F, then to QSBI and/or ESBI, and switches back to ENLSE-5F before the end of the simulations, e.g., Fig. 15(c)(d). It reveals again that the numerical technique for controlling the automatic switch between the three models is also effective for the more complicated cases.

Furthermore, in order to show that the hybrid model successfully captured the movement of the free surface when rogue waves occur, the free surface elevation at focusing time and location for the case $T_f/T_0 = 100\&500\&900$, are shown in Fig. 16. It is seen that no visible difference can be observed between the results obtained by using the hybrid model and the ESBI, which indicates that the hybrid model is very accurate.
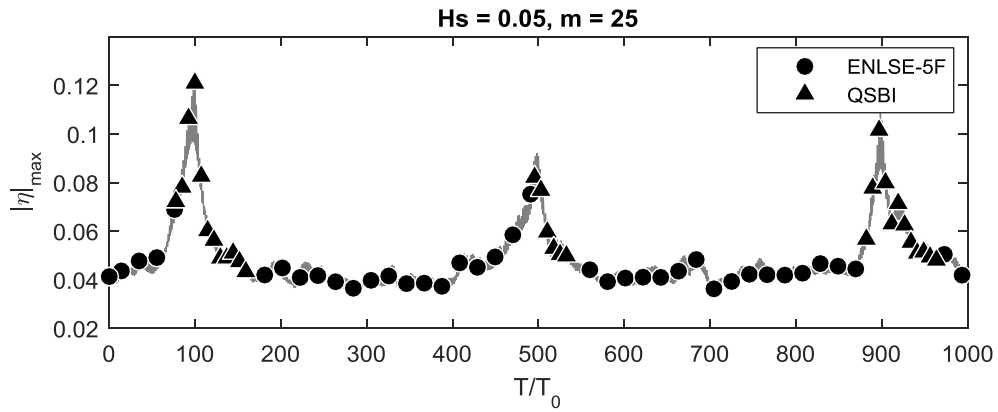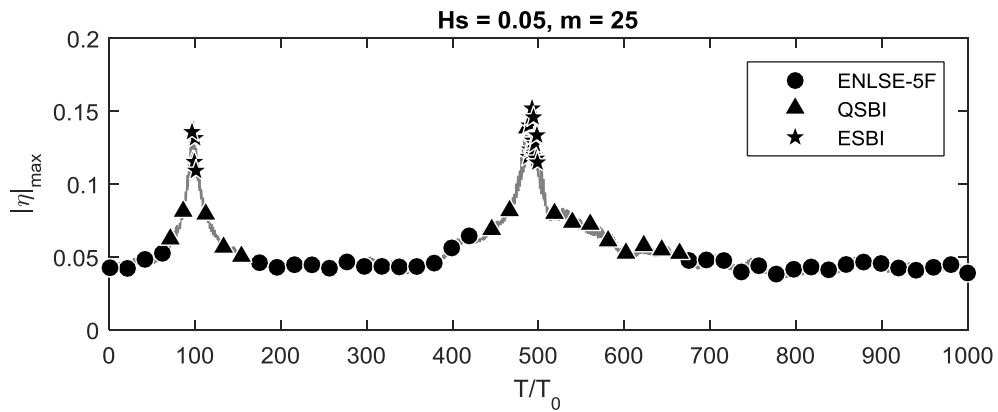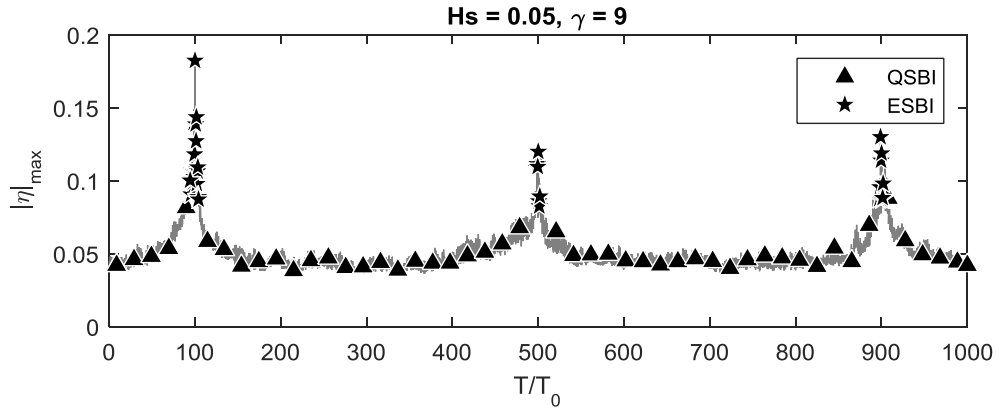

(a): $T_f/T_0 = 100\&500$

(b): $T_f/T_0 = 100\&500\&900$
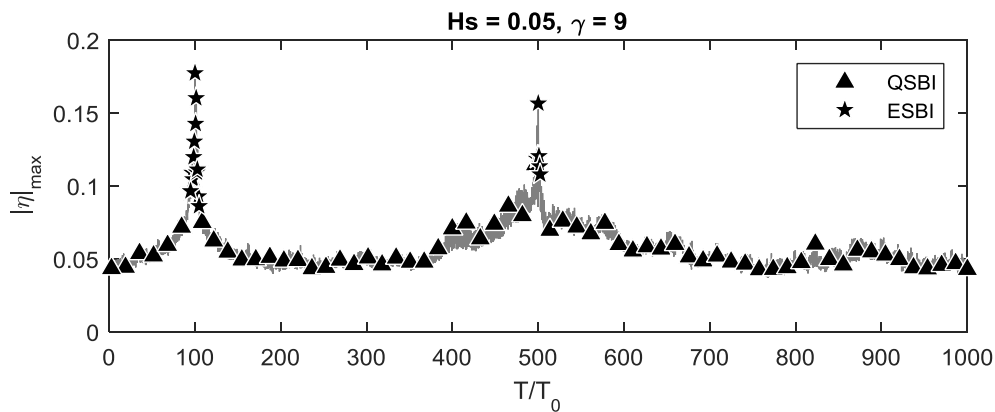
(c): $T_f/T_0 = 100\&500$

(d): $T_f/T_0 = 100\&500\&900$

Fig. 15. Maximum wave elevations with indicator which model is used for the cases of different numbers of rogue waves in time domain
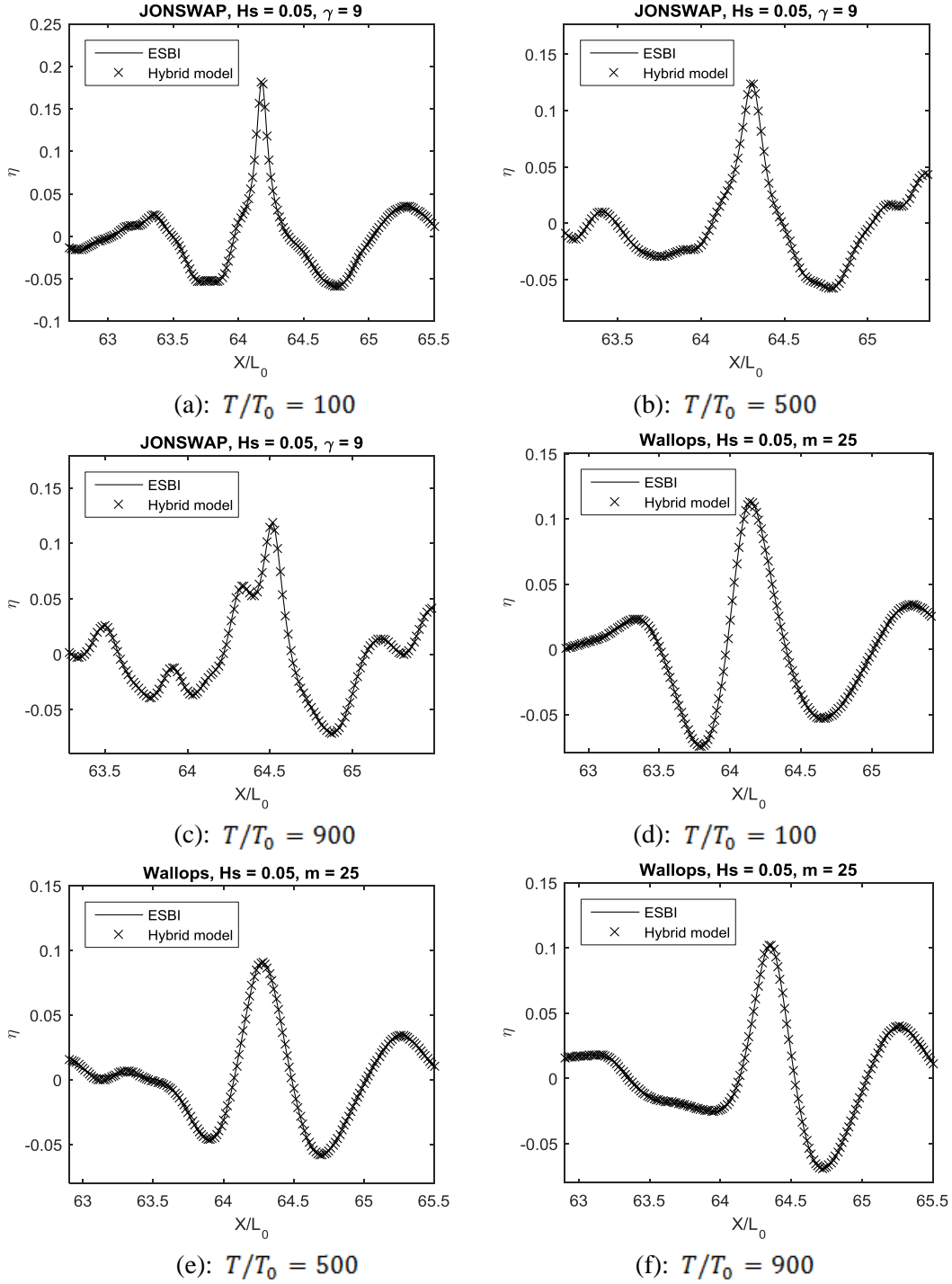
Fig. 16. The profiles of the rogue waves for the cases of different numbers of rogue waves in time domain

4.3 Different numbers of rogue waves in spatial domain

Moreover, there are possibilities that several rogue waves can occur simultaneously but at different locations [9]. Thus in this section, different numbers of rogue waves are generated at $T_f/T_0 = 100$, but at different locations. In addition to the case in which a single rogue wave occurs at $X_f/L_0 = 64$, two more cases of the twins occur at $X_f/L_0 = 32\&64$ and the triplets at $X_f/L_0 = 32\&64\&96$ are investigated. As aforementioned, the rogue wave height

is fixed to $3H_s$ as there will not be energy left to generate the random background if three rogue wave higher than $3H_s$ are generated at the same time by using the method explained in [78]. The basic set-ups are the same with that for Fig. 3 and Fig. 4. Again, the errors and the CPU time ratios are shown in Fig. 17.
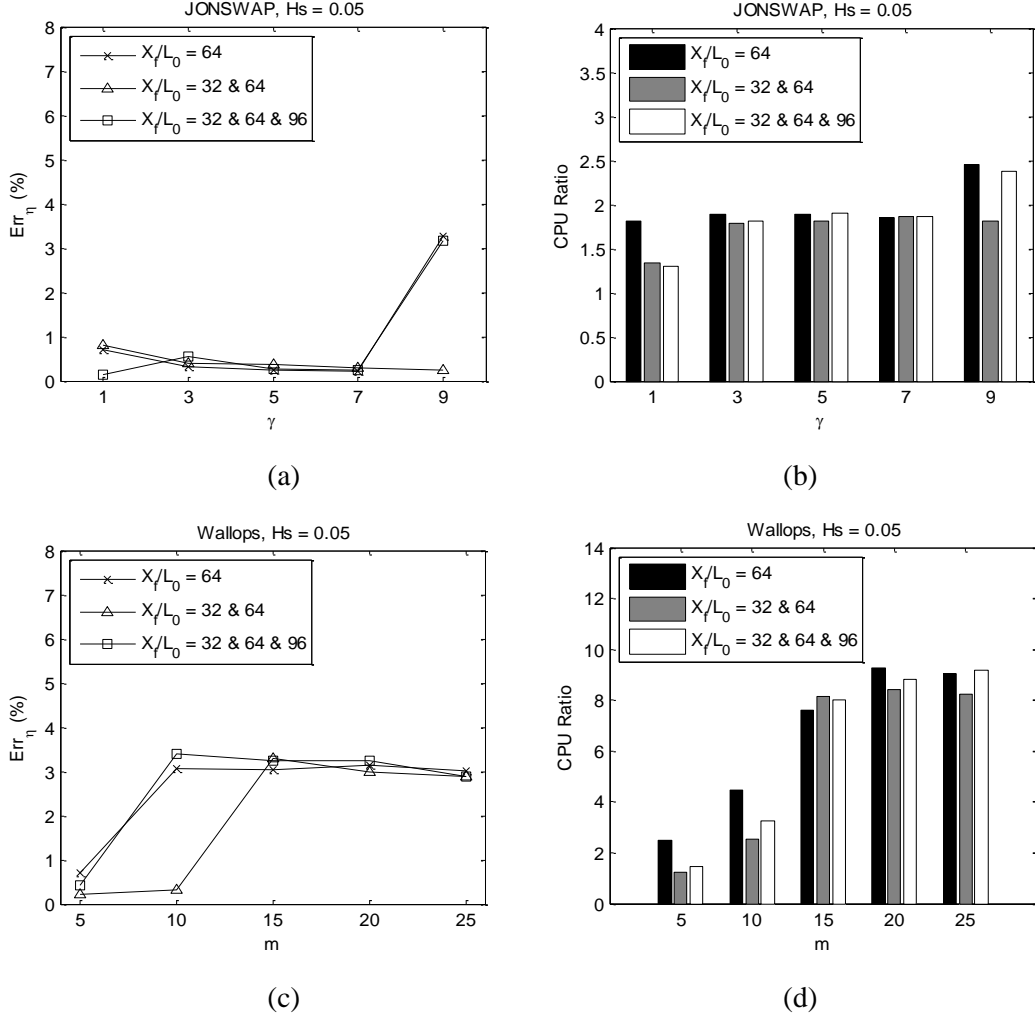

Fig. 17. Err_η and CPU ratio (CPU time of ESBI/CPU time of hybrid model) for the cases of different amount of rogue waves on spatial scale

It is seen again that errors of all simulations considered in this section are less than 5%, which confirms that the values for the Tol_1 and Tol_2 controlling the switch between the models are appropriate for the cases with different embedded rogue waves on spatial scale.

According to Fig. 17(b), for the simulations based on the JONSWAP spectrum, the CPU time ratios reach the highest, i.e., nearly 2.4~2.5, only for the cases $X_f/L_0 = 64$ and $X_f/L_0 = 32\&64\&96$ with $\gamma = 9$, due to the involvement of ENLSE-5F for a limited time steps and QSBI for the most time steps. While for the cases $X_f/L_0 = 32\&64$ and $X_f/L_0 = 32\&64\&96$ with $\gamma = 1$, the majority of the duration is simulated by the ESBI, so that the computational efficiency of the hybrid model is similar to that with the ESBI model

33

alone, which leads to the CPU time ratios approximated equal to 1.3~1.4. In other cases, the majority of the duration is taken over by the QSBI, thus the CPU time ratios are about 1.8, which indicates that the hybrid model still saves almost half the CPU time than the ESBI.

Meanwhile, the situations are totally again different for the simulations based on the Wallops spectrum, as shown in Fig. 17(d), like what has been seen in Fig. 11. The hybrid model is at least 8 time faster than the ESBI alone when $m \geq 10$. In spite of the cases for $X_f/L_0 = 32\&64$ and $X_f/L_0 = 32\&64\&96$ with $m = 5$, in which the CPU time ratios are between 1~1.5, the rest of the cases when $m < 10$ have the CPU time ratios of 2.5~4.5.

The similar graphs to Fig. 6 are also presented in Fig. 18 for these cases, in order to illustrate the effectiveness of the numerical techniques for controlling the switch between each model. It shows that the hybrid model starts with the QSBI and switch to ESBI, then back to QSBI before the end of the simulation in Fig. 18(a). Otherwise, the hybrid model begins with ENLSE-5F, switching to QSBI and/or ESBI when rogue waves occur, then ends with ENLSE-5F or QSBI, e.g., Fig. 18(b)-(d). The various situations shown in Fig. 18 indicate that the hybrid model can start with different models and effectively switch between each other according to the nonlinearities to achieve the highest computational efficiency.

Additionally, the free surface profiles at each focusing location for the case $X_f/L_0 = 32\&64\&96$ are shown in Fig. 19. Although the fully focusing is not achieved at $X_f/L_0 = 96$ in Fig. 19(b), rogue waves are observed at the rest locations. Most importantly, the results obtained by using the hybrid model is consistent with these obtained by using the ESBI, which implies that the hybrid model has successfully captured the movement of the free surface in the complex case.
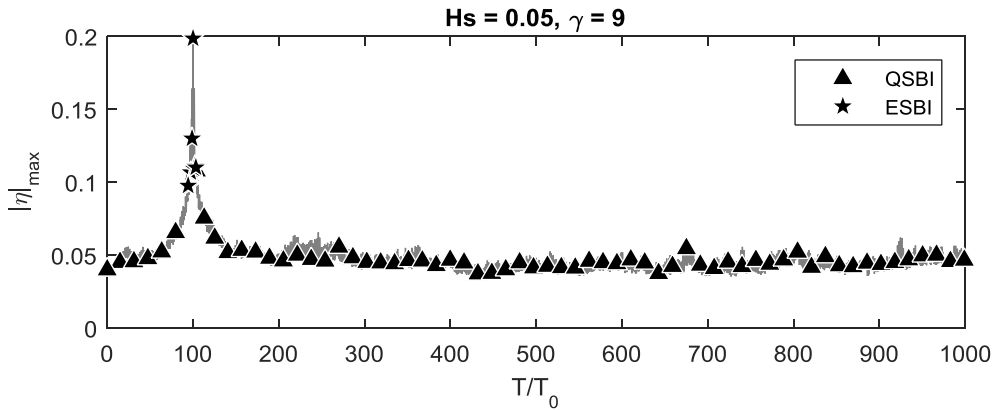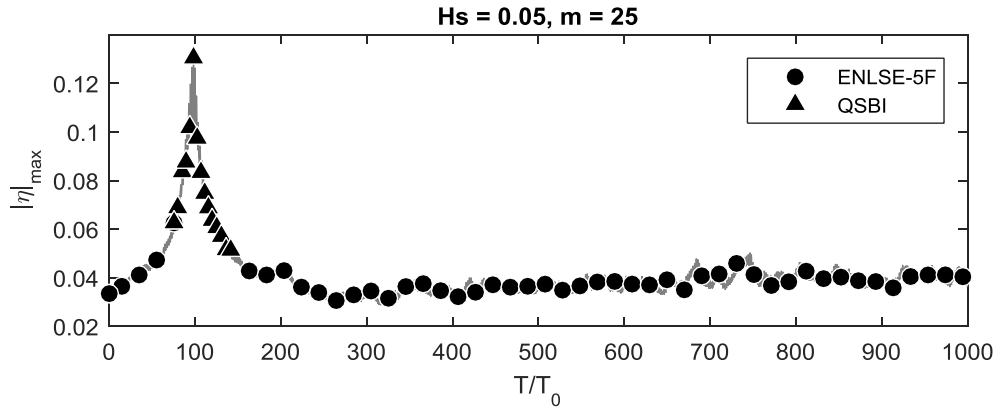

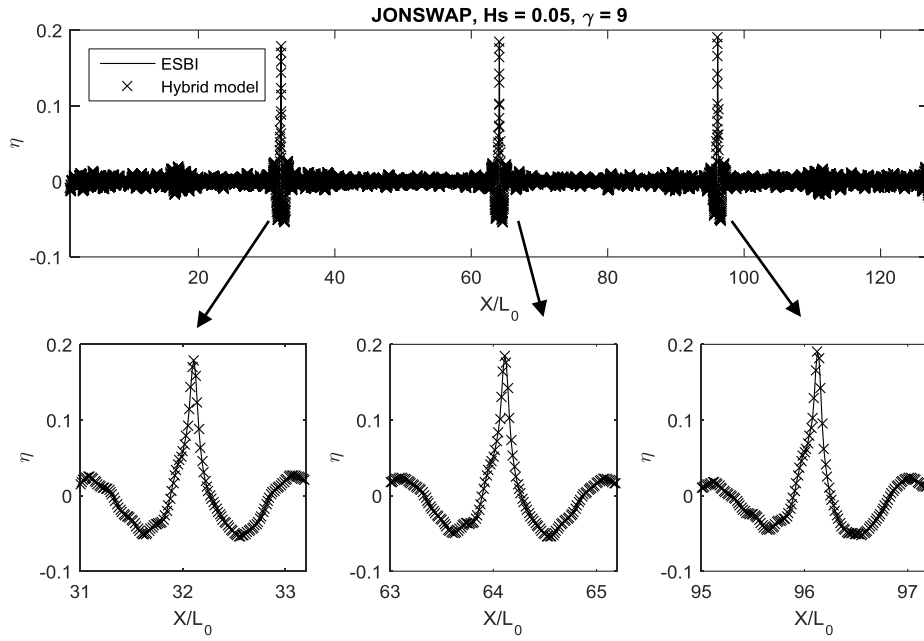(a): $X_f/L_0 = 32\&64$
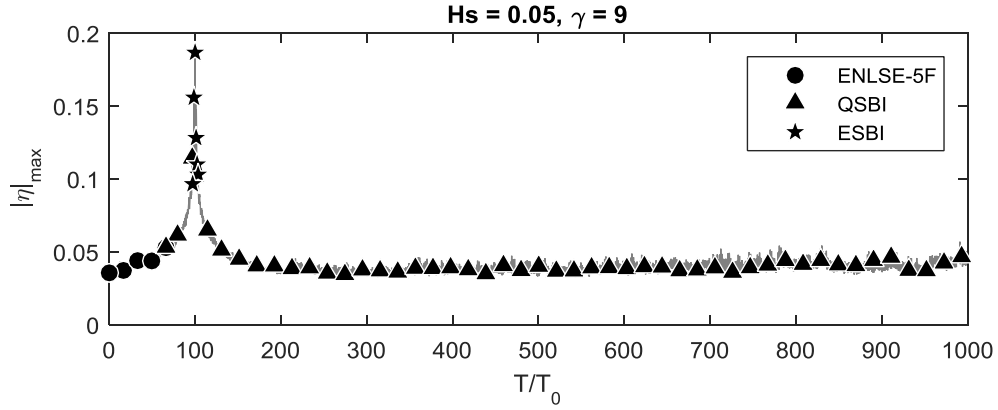
(b): $X_f/L_0 = 32\&64\&96$
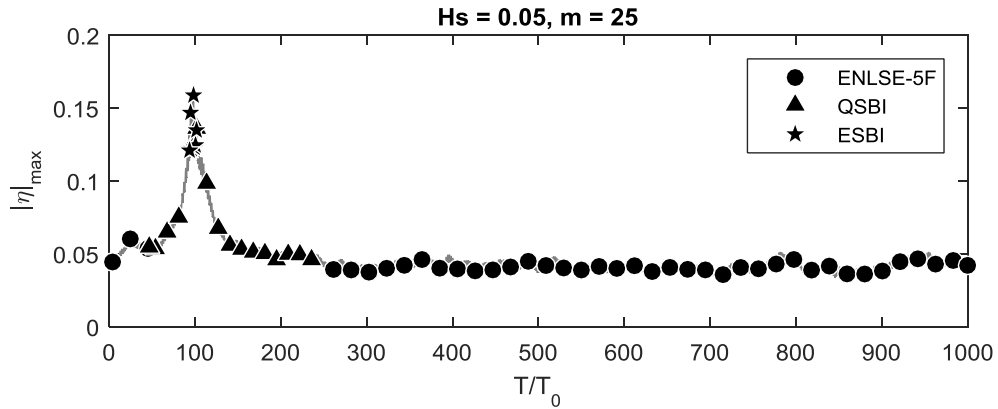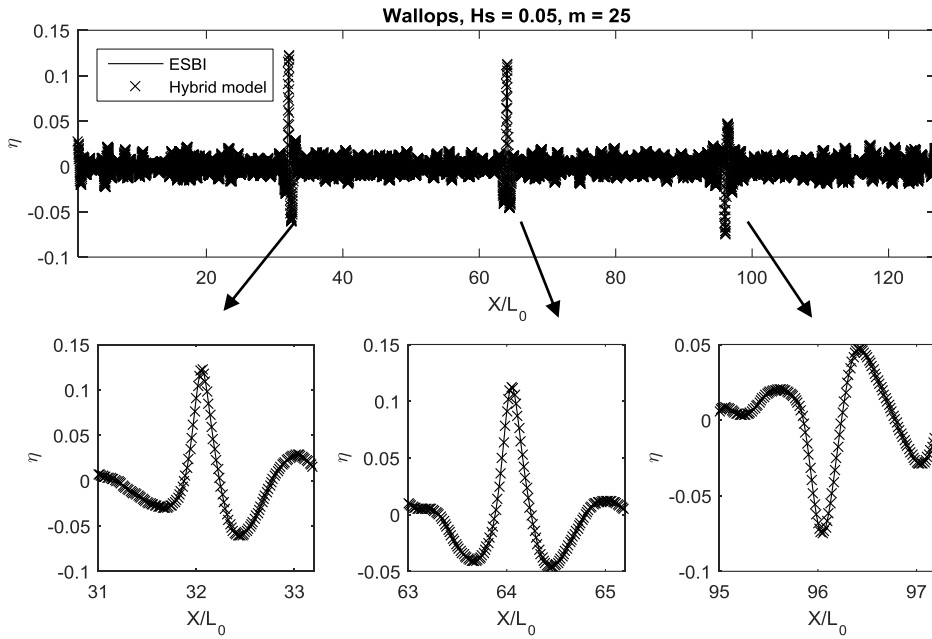

(c): $X_f/L_0 = 32\&64$

(d): $X_f/L_0 = 32\&64\&96$

Fig. 18. Maximum wave elevations with indicator which model is used for the cases of different numbers of rogue waves in spatial domain

(a)

(b)

Fig. 19. The profiles of the rogue waves for the cases of different numbers of rogue waves in spatial domain

4.4 3D random waves simulation

As indicated above, Ducrozet et al. [29] simulated a 3D random sea covering 42×42 peak wave lengths and lasting for 250 peak wave periods by using 10 CPU days on a 3 GHz-Xeon single processor PC based on the fifth order High-order Spectral method. In order to further illustrate the computational efficiency of the present hybrid model, the 3D random

wave simulation in [29] is repeated here, i.e., the computational domain and the duration of wave propagation in our simulation are all the same as in [29]. The free surface elevation is outputted every peak period and it is shown in Fig. 20 for that at $T/T_0 = 250$, and the statistics of the free surface at $T/T_0 = 200$ in comparison with [79] is shown in Fig. 21, which indicates that the results obtained by using the hybrid model is consistent with that in [79]. It is noted that the statistics in [29] for the same case is different from these in [79]. By personal communication with the authors, we are informed that the data in [79] is correct for the case. The simulation of this case is performed by using a single core on a workstation equipped with Intel(R) Xeon(R) CPU E5620@2.4GHz. It is found that only the QSBI and ESBI are involved in the simulation. The total CPU time costed by the hybrid method is 11.9 hours, which is only about 1/20 of the CPU time reported by [29]. In addition, the clock speed of the processor used here is slower than that used by Docrozet et al. [29], which means that the CPU time of the hybrid method can be further reduced if using higher performance computers. It is noted that it is impossible to directly compare our wave elevation with [29] because the phase of each wave component is assigned randomly in both simulations.
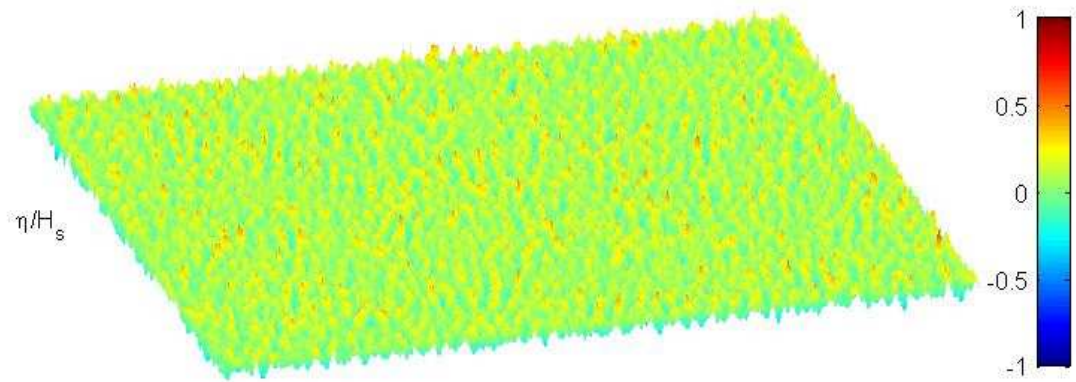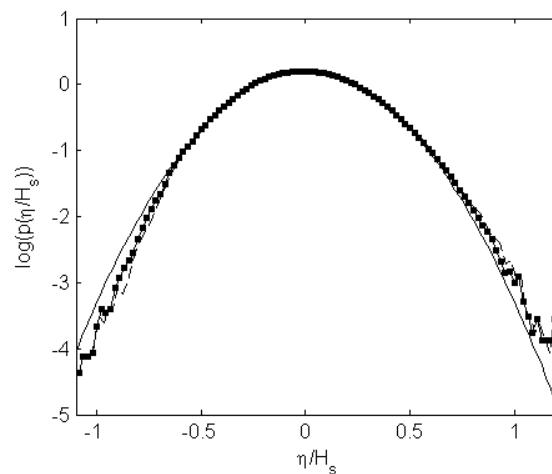

Fig. 20. Free surface elevation at $T/T_0 = 250$

Fig. 21. Probability distribution of free surface elevation at $T/T_0 = 200$. '—' Gaussian

37

Furthermore, two cases of the 3D random sea simulation in [80] (cases (b) and (d) shown in Figure 8 of that paper) are repeated by using the present hybrid model. Following the study in [80], the JONSWAP spectrum and a $\cos^N(\vartheta)$ (with N=50 and 200, respectively) type directional distribution function are used to generate the spreading seas. As an example, the free surface for $N = 200$ at the end of the simulation (after about 60 peak periods) is shown in Fig. 22. The kurtosis estimated by the hybrid method, all larger than 3, is presented in Fig. 23, altogether with the results based on the broader-bandwidth Dysthe equation, HOS method and experimental data in [80]. As well known, the kurtosis represents the contribution of big waves in the statistical distribution, and the contribution of the big waves is significant if it is larger than 3 [9]. It shows in Fig. 23 that the results obtained by using the hybrid model in this paper agrees very well with that obtained based on the HOS method and experimental data in [80]. While the results obtained by using the broader-bandwidth Dysthe equation [80] are significantly smaller. It indicates that the nonlinearities cannot be fully resolved in the simulations based only on the broader-bandwidth Dysthe equation, and in such cases, the fully nonlinear or the hybrid model suggested in this study should be employed.
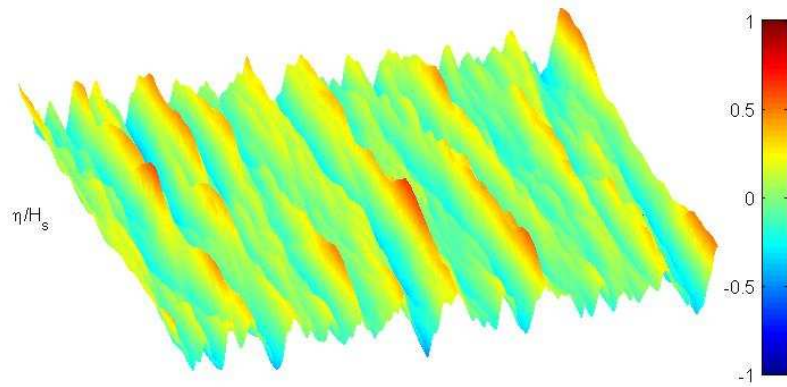

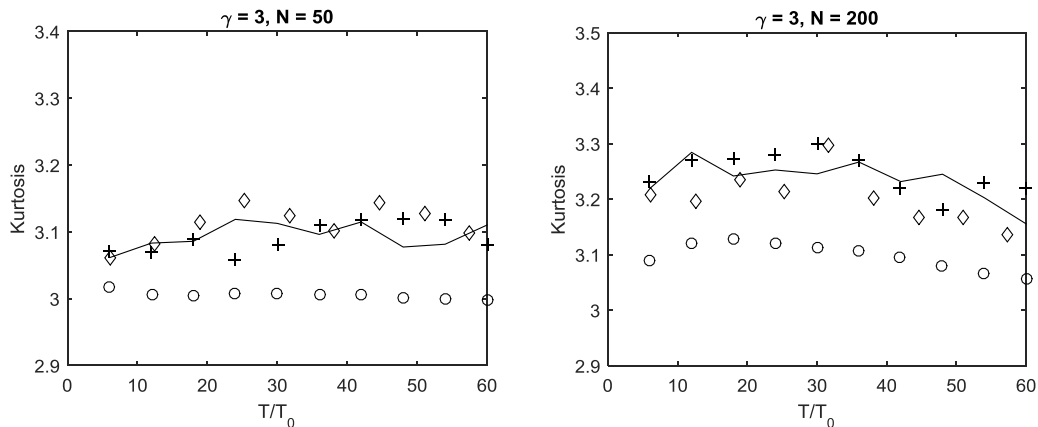**Fig. 22.** Free surface elevation at $T/T_0 = 60$ for $N = 200$

Fig. 23. Kurtosis against time. '—' Hybrid model; 'o' Broader-bandwidth Dysthe equation in [80]; '+' HOS in [80]; '◊' Experiment in [80]

5   Conclusions

This paper presents a new hybrid model for simulating rogue waves in random seas on a large temporal and spatial scale. Firstly, a new formulation (ENLSE-5F) of fifth order Enhanced Nonlinear Schrödinger Equation based on Fourier transform is proposed. The coupling algorithm between the ENLSE-5F, QSBI (Quasi Spectral Boundary Integral) and ESBI (Enhanced Spectral Boundary Integral) methods is then suggested with the techniques for data transfer. The tolerances for controlling the switch between the three models are investigated through numerical tests on the cases corresponding to different spectra with a wide range of parameters. The hybrid method is validated in 2D and 3D cases with the results in literature and these obtained by the fully nonlinear model (ESBI) only. Good agreement between the results is achieved. Various cases are simulated to investigate the effectiveness of the new hybrid method, which include one rogues waves, two rogues and three rogues in time domain and in spatial domain based on two popular wave spectra – Wallops and JONSWAP spectra. The results show that for the same level of accuracy, the hybrid model significantly improved the computational efficiency, especially when the spectrum is narrow. In some cases, the coupled model is more than 10 times faster than just using the ESBI method. For example, in the case with dimensionless significant wave height of $H_s = 0.05$ and dimensionless spectrum bandwidth of $m = 25$ based on the Wallops spectrum embedded with a rogue wave of $2H_s$, the ESBI only requires $2.8h$ while the hybrid model only need $16min$ to finish the simulation. For 3D random waves, we have carried out the simulation of the same case as that in [29], it is found that the CPU time costed by our hybrid method is only about 1/20 of that reported by [29].

Appendix

I.   Analytical solution to the mean flow $\bar{\phi}$

Apply Fourier transform to the last three equations of the system, Eq. (25)-(28), one has

$$\frac{\partial}{\partial Z} F\{\bar{\phi}\} = \frac{1}{2} i\kappa F\{|A|^2\}, \ Z = 0 \tag{A. 1}$$

$$\frac{\partial^2}{\partial Z^2} F\{\bar{\phi}\} = K^2 F\{\bar{\phi}\}, \ Z \le 0 \tag{A. 2}$$

$$\frac{\partial}{\partial Z} F\{\bar{\phi}\} = 0, \ Z = -\infty \tag{A. 3}$$

The second equation admits the solution

$$F\{\bar{\phi}\} = f(\kappa)h(Z) \tag{A. 4}$$

Then $f(\kappa)$ and $g(Z)$ could be given from the boundary conditions as

$$h(Z) = e^{KZ} \tag{A. 5}$$

and

$$f(\kappa) = \frac{i}{2}\frac{\kappa}{K} F\{|A|^2\} \tag{A. 6}$$

Thus

$$F\{\bar{\phi}\} = e^{KZ}\frac{i}{2}\frac{\kappa}{K} F\{|A|^2\} \tag{A. 7}$$

On the surface $Z = 0$, so that

$$\bar{\phi} = F^{-1}\left\{\frac{i}{2}\frac{\kappa}{K} F\{|A|^2\}\right\} \tag{A. 8}$$

II. Relationship between the Hilbert and Fourier transforms

Note that Eq. (37) could be rewritten as

$$\mathcal{H}\{f(X)\} = \frac{1}{2\pi}\frac{\partial}{\partial X}\int_{-\infty}^{\infty} f(X')\frac{1}{|X' - X|}dX' \tag{A. 9}$$

One also has the Fourier transform

$$F\left\{\frac{1}{|X|}\right\} = \frac{2\pi}{K} \quad and \quad F\left\{\frac{X}{|X|^2}\right\} = -\frac{2\pi i\kappa}{K^2} \tag{A. 10}$$

where $K = |K|$ and $K = (\kappa, \zeta)$, thus

$$F\left\{\frac{1}{|X' - X|}\right\} = \int_{-\infty}^{\infty}\frac{1}{|X - X'|}e^{-iK\cdot X}dX$$
$$= e^{-iK\cdot X'}\int_{-\infty}^{\infty}\frac{1}{|X - X'|}e^{-iK\cdot(X-X')}dX = \frac{2\pi}{K}e^{-iK\cdot X'} \tag{A. 11}$$

Similarly

$$F\left\{\frac{X' - X}{|X' - X|^2}\right\} = -e^{-iK\cdot X'}\int_{-\infty}^{\infty}\frac{X - X'}{|X - X'|^2}e^{-iK\cdot(X-X')}dX = \frac{2\pi i\kappa}{K^2}e^{-iK\cdot X'} \tag{A. 12}$$

Replace the Hilbert transform coefficients in both the expressions in Eq. (37) and (38) after applying Fourier transform on both sides, one has

$$F\{\mathcal{H}\{f(X)\}\} = \frac{1}{2\pi}i\kappa\int_{-\infty}^{\infty} f(X')F\left\{\frac{1}{|X' - X|}\right\}dX'$$
$$= \frac{1}{2\pi}i\kappa\int_{-\infty}^{\infty} f(X')\frac{2\pi}{K}e^{-iK\cdot X'}dX' = i\frac{\kappa}{K}F\{f(X)\} \tag{A. 13}$$

$$F\{\mathcal{P}\{f(X)\}\} = \frac{1}{2\pi}\int_{-\infty}^{\infty}f(X')F\left\{\frac{X'-X}{|X'-X|^2}\right\}dX'$$

$$= \frac{1}{2\pi}\int_{-\infty}^{\infty}f(X')\frac{2\pi i\kappa}{K^2}e^{-iK\cdot X'}dX' = \frac{i\kappa}{K^2}F\{f(X)\}$$

(A. 14)

III. The harmonic coefficients in terms of A

Trulsen and Dysthe [43] have given the coefficients for each harmonic of the surface elevation and velocity potential, corresponding to the first kind of NLSE in terms of B, which follow as

$$A = iB + \frac{1}{2}\frac{\partial B}{\partial X} + \frac{i}{8}\frac{\partial^2 B}{\partial X^2} - \frac{i}{4}\frac{\partial^2 B}{\partial Y^2} - \frac{1}{16}\frac{\partial^3 B}{\partial X^3} - \frac{3}{8}\frac{\partial^3 B}{\partial X\partial Y^2} - \frac{5i}{128}\frac{\partial^4 B}{\partial X^4}$$
$$+ \frac{15i}{32}\frac{\partial^4 B}{\partial^2 X\partial Y^2} - \frac{3i}{32}\frac{\partial^4 B}{\partial Y^4} + \frac{i}{8}|B|^2 B$$

(A. 15)

$$A_2 = -\frac{1}{2}B^2 + iB\frac{\partial B}{\partial X} + \frac{1}{8}B\frac{\partial^2 B}{\partial X^2} + \frac{3}{8}\left(\frac{\partial B}{\partial X}\right)^2 - \frac{1}{4}B\frac{\partial^2 B}{\partial Y^2} + \frac{3}{4}\left(\frac{\partial B}{\partial Y}\right)^2$$

(A. 16)

$$A_3 = -\frac{3i}{8}B^3$$

(A. 17)

$$B_2 = \frac{i}{2}B\frac{\partial^2 B}{\partial Y^2} - \frac{i}{2}\left(\frac{\partial B}{\partial Y}\right)^2$$

(A. 18)

$$B_3 = 0$$

(A. 19)

$$\bar{\eta} = -\bar{\phi}_T - \frac{1}{16}\frac{\partial^2|B|^2}{\partial X^2} - \frac{1}{8}\frac{\partial^2|B|^2}{\partial Y^2}$$

(A. 20)

However, since the ENLSE-5F in this study is an equation in terms of A, the solution by using Eq.(A. 15) - (A. 20) is not straightforward. According to Hogan's substitution [69], i.e., $B = -iA + 0.5\partial A/\partial X$, replace which into the expression for each harmonic coefficient and keep the appearance to the fourth order, then we have for Eq. (A. 16)

$$A_2 = \frac{1}{2}A^2 - \frac{i}{2}A\frac{\partial A}{\partial X} + \frac{3}{8}A\frac{\partial^2 A}{\partial X^2} + \frac{1}{4}A\frac{\partial^2 A}{\partial Y^2} - \frac{3}{4}\left(\frac{\partial A}{\partial Y}\right)^2$$

(A. 21)

For Eq. (A. 17)

$$A_3 = -\frac{3i}{8}B^3 = -\frac{3i}{8}\left(-A^2 - iA\frac{\partial A}{\partial X}\right)\left(-iA + \frac{1}{2}\frac{\partial A}{\partial X}\right) \approx \frac{3}{8}A^3$$

(A. 22)

For Eq.(A. 20), where

$$|B|^2 = \left(-iA + \frac{1}{2}A_X\right)\left(iA^* + \frac{1}{2}A_X^*\right) \approx |A|^2 - \frac{i}{2}AA_X^* + \frac{i}{2}A^*A_X$$

(A. 23)

Substitute Eq.(A. 23) and Eq.(A. 8) into Eq. (A. 20) and neglecting higher order terms

$$\bar{\eta} = F^{-1}\left\{-i\frac{\kappa}{K}F\{real(A^*A_T)\}\right\} - \frac{1}{16}\frac{\partial^2|A|^2}{\partial X^2} - \frac{1}{8}\frac{\partial^2|A|^2}{\partial Y^2} \qquad (A.\,24)$$

Now all the harmonic coefficients are obtained for transforming A to η, next the coefficients for transforming A to ϕ will be introduced. Since $\bar{\phi}$ has already been obtained as given by Eq. (A. 8), and $B_3 = 0$, the first and second harmonic coefficient for velocity potential are the only variables remain unknown, which will be formulated.

Based on the NLSE of first kind to the 3rd order [38], i.e.,

$$\frac{1}{2}\frac{\partial B}{\partial X} + \frac{i}{8}\frac{\partial^2 B}{\partial X^2} - \frac{1}{16}\frac{\partial^3 B}{\partial X^3} = -\frac{\partial B}{\partial T} - \frac{i}{2}|B|^2 B \qquad (A.\,25)$$

substitute which into Eq. (A. 15), one has

$$A = iB - \frac{\partial B}{\partial T} - \frac{3i}{8}|B|^2 B \qquad (A.\,26)$$

This expression is consistent with Mei's deduction [68]. Meanwhile, the exact linear solution admits

$$\frac{\partial B}{\partial T} = F^{-1}\{i(1-\omega)F\{B\}\} \qquad (A.\,27)$$

substitute which into Eq. (A. 26),

$$A = F^{-1}\{i\omega F\{B\}\} - \frac{3i}{8}|B|^2 B \qquad (A.\,28)$$

Re-arrange Eq. (A. 28)

$$F^{-1}\{i\omega F\{B\}\} = A + \frac{3i}{8}|B|^2 B \approx A + \frac{3}{8}|A|^2 A \qquad (A.\,29)$$

and make B explicit

$$B = F^{-1}\left\{\frac{-i}{\omega}F\left\{A + \frac{3}{8}|A|^2 A\right\}\right\} \qquad (A.\,30)$$

Now the first harmonic coefficient B for velocity potential is obtained. Similarly, the second harmonic coefficient for the velocity potential can be reformulated as

$$B_2 = -\frac{i}{2}A\frac{\partial^2 A}{\partial Y^2} + \frac{i}{2}\left(\frac{\partial A}{\partial Y}\right)^2 \qquad (A.\,31)$$

IV. Transformation from free surface η_1 to envelope A

It is known that

$$\eta_1 = \frac{1}{2}\left[Ae^{i(X-T)} + c.c.\right] \qquad (A.\,32)$$

The 1st harmonic could also be described as the summation of various components

$$\eta_1 = \sum_{j=1}^{N/2} \frac{1}{2}\left(\Lambda_j e^{iK_j X} + c.c.\right) \tag{A.33}$$

If we assume $\Lambda_j = p_j + iq_j$, where p and q are real functions of X. Then

$$\eta_1 = \sum_{j=1}^{N/2} \frac{1}{2}\left(\Lambda_j e^{iK_j X} + c.c.\right) = \sum_{j=1}^{N/2}\left(p_i \cos(K_j X) + q_i \sin(K_j X)\right) \tag{A.34}$$

Applying 1D Hilbert transform $\hbar\{\eta_1(X)\} = \pi^{-1}\int_{-\infty}^{\infty}\eta_1(X')/(X'-X)\,dX'$ to η_1 gives

$$\hbar\{\eta_1\} = \sum_{j=1}^{N/2}\left(-p_i \sin(K_j X) + q_i \cos(K_j X)\right) \tag{A.35}$$

Therefore

$$\begin{aligned}
\sum_{j=1}^{N/2}\Lambda_j e^{iK_j X} &= \sum_{j=1}^{N/2}\big[p_i \cos(K_j X) + q_i \sin(K_j X) \\
&\quad - i\left(-p_i \sin(K_j X) + q_i \cos(K_j X)\right)\big] = \eta_1 - i\hbar\{\eta_1\} \\
&= Ae^{i(X-T)}
\end{aligned} \tag{A.36}$$

Thus

$$A = e^{-i(X-T)}\left(\eta_1 - i\hbar\{\eta_1\}\right) \tag{A.37}$$

Note that $\hbar\{\eta_1\} = F^{-1}\{i\,sgn(\kappa)F\{\eta_1\}\}$, then the equation above becomes

$$\begin{aligned}
A &= e^{-i(X-T)}\left(\eta_1 - iF^{-1}\{i\,sgn(\kappa)F\{\eta_1\}\}\right) \\
&= e^{-i(X-T)}\left(\eta_1 + F^{-1}\{sgn(\kappa)F\{\eta_1\}\}\right)
\end{aligned} \tag{A.38}$$

Acknowledgements

References

[1] G. B. Airy, Tides and waves, London: Encyclopaeida Metropolitana, 1845.

[2] H. Lamb, Hydrodynamics (Fourth Edition), Cambridge: Cambrige University Press, 1916.

[3] J. Lighthill, Waves in Fluids, London: Cambridge University Press, 1978.

[4] G. G. Stokes, On the theory of oscillatary waves, London: Cambridge University Press, 1847.

[5] T. B. Benjamin and J. E. Feir, "The disintegration of wave trains on deep water Part 1. Theory," J. Fluid Mech., vol. 2, pp. 417-430, 1967.

[6] P. C. Liu, "A chronology of freauqe wave encounters," Geofizika, vol. 24, no. 1, pp. 57-70, 2007.

[7] I. Nikolkina and I. Didenkulova, "Catalogue of rogue waves reported in media in 2006-2010," Natural hazards, vol. 61, no. 3, pp. 989-1006, 2012.

[8] J. Skourup, N. Ottensen Hansen and K. Andreasen, "Non-Gaussian Extreme Waves in the Central North Sea," Proc. Offshore Mechanics and Arctic Engineering Conf., Vols. I-A, pp. 25-32, 1996.

[9] C. Kharif, E. Pelinovsky and A. Slunyaev, Rogue Waves in the Ocean, Berlin Heidelberg: Springer-Verlag, 2009.

[10] T. A. Adcock and P. H. Taylor, "The physics of anomalous ('rogue') ocean waves," Reports on Progress in Physics, vol. 77, no. 10, p. 105901, 2014.

[11] D. J. Korteweg and G. DE Vries, "On the change of form of long waves advancing in a rectangular cannal, and on a new type of long stationary waves," Phil. Mag., vol. 39, pp. 422-443, 1895.

[12] J. Boussinesq, " Théorie de l'intumescence liquide, applelée onde solitaire ou de translation, se propageant dans un canal rectangulaire," Comptes Rendus de l'Academie des Sciences, vol. 72, pp. 755-759, 1871.

[13] D. Kriebel, "Nonlinear wave interaction with a vertical circular cylinder. Part I: Diffraction theory," Ocean Engineering, vol. 17, no. 4, pp. 345-377, 1990.

[14] D. Kriebel, "Nonlinear wave interaction with a vertical circular cylinder. Part II: Wave run-up," Ocean Engineering, vol. 19, no. 1, pp. 75-99, 1992.

[15] M. Onorato, A. R. Osborne, M. Serio, L. Cavaleri, C. Brandini and C. Stansberg, "Extreme waves, modulational instability and second order theory: wave flume experiments on irregular waves," European Journal of Mechanics-B/Fluids, vol. 25, no. 5, pp. 586-601, 2006.

[16] O. M. Phillips, "Wave interactions - the evolution of an idea," Journal of Fluid Mechanics, vol. 106, pp. 215-227, 1981.

[17] R. S. Gibson and C. Swan, "The evolution of large ocean waves: the role of local and rapid spectral changes," Proceedings of the Royal Society of London A: Mathematical, Physical and Engineering Sciences, vol. 463, no. 2077, pp. 21-48, 2007.

[18] D. Z. Ning, J. Zang, S. X. Liu, R. E. Taylor, B. Teng and P. H. Tanlor, "Free-surface evolution and wave kinematics for nonlinear uni-directional focused wave groups," Ocean Engineering, vol. 36, no. 15, pp. 1226-1243, 2009.

[19] F. H. Harlow and J. E. Welch, "Numerical Calculation of Time-Dependent Viscous Incompressible Flow of Fluid with Free Surface," Physics of Fluids, vol. 8, pp.

2182-2189, 1965.

[20] C. W. Hirt and B. D. Nichols, "Volume of fluid (VOF) method for the dynamics of free boundaries," Journal of Computational Physics, vol. 39, no. 1, pp. 201-225, 1981.

[21] J. Touboul, J. P. Giovanangeli, C. Kharif and E. Pelinovsky, "Freak waves under the action of wind: experiments and simulations," European Journal Mechanics B/Fluid, vol. 25, pp. 662-676, 2006.

[22] S. Yan and Q. W. Ma, "Improved model for air pressure due to wind on 2D freak waves in finite depth," European Journal Mechanics B/Fluid, vol. 30, pp. 1-11, 2011.

[23] J. Touboul, E. Pelinovsky and C. Kharif, "Nonlinear focusing wave group on current," Journal of Korean Society of Coastal and Ocean Engineers, vol. 19, pp. 222-227, 2007.

[24] S. Yan, Q. W. Ma and T. A. A. Adcock, "Investigation of freak waves on uniform current," in Proceeding of 25th international workshop on water waves and floating bodies, Harbin, 2010.

[25] G. F. Clauss, C. E. Schmittner and R. Stuck, "Numerical wave tank - simulation of extreme waves for the investigation of structural responses," in 24th International Conference on Offshore Mechanics and Arctic Engineering, Halkidiki, Greece, 2005.

[26] S. Yan, Numerical simulation on nonlinear response of moored floating structures to steep waves (PhD thesis), London, UK: School of Engineering and Mathematical Sciences, City University London, 2006.

[27] W. Xiao, Study of directional ocean wavefield evolution and rogue wave occurrence using large-scale phase-resolved nonlinear simulations (Doctoral dissertation), Cambridge, United States: Massachusetts Institute of Technology, 2013.

[28] Y. Goda, Random Seas and Design of Maritime Structures, Singapore: World Scientific, 2010.

[29] G. Ducrozet, E. Bonnefoy, D. L. Touze and P. Ferrant, "3-D HOS simulation of extreme waves in open seas," Nat. Hazards Earth Syst. Sci., vol. 7, pp. 109-122, 2007.

[30] K. Hasselmann, T. P. Barnerr, E. Bouws, H. Carlson, D. E. Cartwright, K. Enke, J. A. Ewing, H. Gienapp, D. E. Hasselmann, P. Kruseman, A. Meerburg, P. Muller, D. J. Olbers, K. Richter, W. Sell and H. Walden, "Measurements of wind-wave growth and swell decay during the joint north sea wave project (JONSWAP)," Deutsches Hydrographisches, Hamburg, 1973.

[31] G. Wu, Direct Simulation and Deterministic Prediction of Large-scale Nonlinear Ocean Wave-field (PhD Thesis), Massachusetts, USA: Massachusetts Institute of Technology, 2004.

[32] G. Z. Forristall, "Understanding rogue waves: Are new physics really necessary?," in Proc. 14th Aha Huliko's Winter Workshop, Honolulu, Hawaii, 2005.

[33] F. Ursell, "The long wave paradox in the theory of gravity waves," Proc. Cambridge Phil. Soc., vol. 49, pp. 685-694, 1953.

[34] G. Wei, J. T. Kirby, S. T. Grilli and R. Subramanya, "A fully nonlinear Boussinesq model

for suface waves. Part 1. Highly nonlinear unsteady waves," J. Fluid Mech., vol. 294, pp. 71-92, 1995.

[35] P. A. Madsen, H. B. Bingham and H. A. Schäffer, "Boussinesq-type formulations for fully nonlinear and extremely dispersive water waves: derivation and analysis," Proc. R. Soc. Lond. A, vol. 459, no. 2033, pp. 1075-1104, 2003.

[36] P. J. Lynett and P. L. F. Liu, "Linear analysis of the multi-layer model," Coastal Engineering, vol. 51, pp. 439-454, 2004.

[37] P. A. Madsen and D. R. Fuhrman, "High-Order Boussinesq-Type Modelling of Nonlinear Wave Phenomena in Deep and Shallow Water," in Adcances in Numerical Simulation of Nonlinear Water Waves, Singagpore, World Scienticif Publishing Co. Pte. Ltd., 2010, pp. 245-286.

[38] V. E. Zakharov, "Stability of periodic waves of finite amplitude on the surface of a deep fluid," Sov. Phys. J. Appl. Mech. Tech. Phys, vol. 9, pp. 86-94, 1968.

[39] D. J. Benney and G. J. Roskes, "Wave instabilities," Studies in Applied Mathematics, vol. 48, pp. 377-385, 1969.

[40] H. Hasimoto and H. Ono, "Nonlinear modulation of gravity waves," Journal of the Physical Society of Japan, vol. 33, pp. 805-811, 1972.

[41] A. Davey and K. Stewartson, "On three-dimensional packets of surface waves," Proc. R. Soc. Lond. A, vol. 388, pp. 101-110, 1974.

[42] K. B. Dysthe, "Note on a modification to the nonlinear Schrödinger equation for application to deep water waves," Proc. R. Soc. Lond. A, vol. 369, pp. 105-114, 1979.

[43] K. Trulsen and K. B. Dysthe, "A modified nonlinear Schrödinger equation for broader bandwidth gravity waves on deep water," Wave motion, vol. 24, pp. 281-298, 1996.

[44] K. Trulsen, I. Kliakhandler, K. B. Dysthe and M. G. Velarde, "On weakly nonlinear modulation of waves on deep water," Physics of Fluids, vol. 12 , no. 10, pp. 2432-2437, 2000.

[45] M. Stiassnie, "Note on the modified nonlinear Schrödinger equation for deep water waves," Wave Motion, vol. 6, pp. 431-433, 1984.

[46] S. Debsarma and K. P. Das, "A higher-order nonlinear evolution equation for broader bandwidth gravity waves in deep water," Physics of Fluids, vol. 14, no. 104101, pp. 1-8, 2005.

[47] K. Dysthe, H. Socquet-Juglard, K. Trulsen, H. Krogstad and J. Liu, ""Freak" waves and large-scale simulations of surface gravity waves," in *Proc. 14th 'Aha Huliko' a Hawaiian Winter Workshop*, Honolulu, Hawaii, 2005.

[48] M. Onorato, D. Proment and A. Toffoli, "Triggering rogue waves in opposing currents," Phys. Rev. Lett., vol. 107, no. 18, pp. 184502-184507, 2011.

[49] L. Shemer, A. Sergeeva and A. Sunyaev, "Applicability of envelope model equations for simulation of narrow-spectrum unidirectional random wave field evolution: Experimental validation," Physics of Fluids, vol. 22, pp. 016601 1-9, 2010.

[50] M. Onorato, A. R. Osborne, M. Serio and S. Bertone, "Freak waves in random oceanic sea states," Physical review letters, vol. 86, no. 25, pp. 5831-5834, 2001.

[51] Y. Zhang, N. Zhang and Y. Pei, "Numerical simulation and mechanism analysis of freak waves in random ocean sea states," in Proceedings of the Seventeenth (2007) International Offshore and Polar Engineering Conference, Lisbon, Portugal, 2007.

[52] M. S. Longuet-Higgins and E. D. Cokelet, "The deformation of steep surface waves on water. I. A numerical method of computation," Pro. R. Soc. Lond. A, vol. 350, pp. 1-26, 1976.

[53] S. T. Grilli, P. Guyenne and F. Dias, "A fully non-linear model for three-dimensional overturning waves over an arbitrary bottom," International Journal for Numerical Methods in Fluids, vol. 35, pp. 829-867, 2001.

[54] G. X. Wu and R. Eatock-Taylor, "Finite element analysis of two dimensional non-linear transient water waves," Appl. Ocean Res., vol. 16, pp. 363-372, 1994.

[55] Q. W. Ma, Numerical simulation of nonliear interaction between structures and steep waves (PhD Thesis), London: Department of Mechanical Enginieering, University College London, UK, 1998.

[56] Q. W. Ma and S. Yan, "Quasi ALE finite element method for nonlinear water waves," Journal of Computational Physics, vol. 212, pp. 52-72, 2006.

[57] B. West, K. Brueckner, R. Janda, D. Milder and R. Milton, "A new numerical method for surface hydrodynamics," Journal of Geophysical Research: Oceans, vol. 92, no. C11, pp. 11803-11824, 1978.

[58] D. G. Dommermuth and D. K. P. Yue, "A high-order spectral method for the study of nonlinear gravity waves," J. Fluid Mech., vol. 184, pp. 267-288, 1987.

[59] D. P. Nicholls, "Traveling Water Waves: Spectral Continuation Methods with Parallel Implementation," Journal of Computational Physics, vol. 143, no. 1, pp. 224-240, 1998.

[60] D. Clamond and J. Grue, "A fast method for fully nonlinear water-wave computations," J. Fluid Mech., vol. 447, pp. 337-355, 2001.

[61] D. Fructus, D. Clamond, J. Grue and O. Kristiansen, "An efficient model for three-dimensional surface wave simulations Part I: Free space problems," Journal of Computational Physics, vol. 205, pp. 665-685, 2005.

[62] J. Grue, "Computation formulas by FFT of the nonlinear orbital velocity in three-dimensional surface wave fields," J. Eng. Math., vol. 67, pp. 55-69, 2010.

[63] J. Wang and Q. W. Ma, "Numerical techniques on improving computational efficiency of Spectral Boundary Integral Method," International Journal for Numerical Methods in Engineering, vol. 102, no. 10, p. 1638–1669, 2015.

[64] D. Clamond, M. Francius, J. Grue and C. Kharif, "Long time interaction of envelope solitons and freak wave formations," European Journal of Mechanics B/Fluids, vol. 25, pp. 536-553, 2006.

[65] W. Xiao, Y. Liu, G. Wu and D. K. P. Yue, "Rogue wave occurrence and dynamics by

direct simulations of nonlinear wave-field evolution," J. Fluid Mech., vol. 720, pp. 357-392, 2013.

[66] K. L. Henderson, D. H. Peregrine and J. W. Dold, "Unsteady water wave modulations: fully nonlinear solutions and comparison with the nonlienar Schrodinger equation," Wave Motion, vol. 29, pp. 341-361, 1999.

[67] A. Slunyaev, E. Pelinovsky, A. Sergeeva, A. Chabchoub, N. Hoffmann, M. Onorato and N. Akhmediev, "Super rogue waves in simulations based on weakly nonlinear and fully nonlinear hydrodynamic equations," Physical Review E, vol. 88, no. 1, p. 012909, 2013.

[68] C. Mei, The applied dynamics of ocean surface waves, New York: Wiley, 1983.

[69] S. J. Hogan, "The fourth-order evolution equation for deep-water gravity-capillary waves," Proc. R. Soc. Lond. A, vol. 402, pp. 359-372, 1985.

[70] N. E. Huang, S. R. Long, C.-C. Tung, Y. Yuen and L. F. Bliven, "A unified two-parameter wave spectral model for a general sea state," J. Fluid Mech. , vol. 112, pp. 203-224, 1981.

[71] Y. Goda, "A comparative review on the functional forms of directional wave spectrum," Coastal Engineering Journal, vol. 41, no. 1, pp. 1-20, 1999.

[72] W. J. D. Bateman, C. Swan and P. H. Taylor, "On the efficient numerical simulation of directionally spread surface water waves," J. Comput. Phys., vol. 174, pp. 277-305, 2001.

[73] P. H. Taylor, J. Philip and A. H. Léon, "Time domain simulation of jack-up dynamics with the extremes of a Gaussian process," Journal of vibration and acoustics, vol. 119, no. 4, pp. 624-628, 1997.

[74] D. Fructus, C. Kharif, M. Francius, Ø. Kristiansen, D. Clamond and J. Grue, "Dynamics of crescent water wave patterns," Journal of Fluid Mechanics, vol. 537, pp. 155-186, 2005.

[75] G. F. Clauss and U. Steinhagen, "Optimization of Transient Design Waves in Random Sea," in Proceedings of the Tenth (2000) International Offshore and Polar Engineering Conference, Seatle, USA, 2000.

[76] C. H. Kim, Nonlinear Waves and Offshore Structure, Singapore: World Scientific Publishing Co. Pte. Ltd, 2008.

[77] D. L. Kriebel and M. V. Alsina, "Simulation of Extreme Waves in a Background Random Sea," in Proceedings of the Tenth (2000) International Offshore and Polar Engineering Conference, Seatle, USA, 2000.

[78] J. Wang, S. Yan and Q. W. Ma, "An Improved Technique to Generate Rogue Waves in Random Sea," CMES: Computer Modeling in Engineering & Sciences, vol. 106, no. 4, pp. 263-289, 2015.

[79] G. Docruzet, Modélisation des processus non-linéaires de génération et de propagation d'états de mer par une approche spectrale (Doctoral dissertation), Ecole Centrale de Nantes: Université de Nantes, 2007.

[80] A. Toffoli, O. Gramstad, K. Trulsen, J. Monbaliu, E. Bitner-Gregersen and M. Onorato, "Evolution of weakly nonlinear random directional waves: laboratory experiments and numerical simulations," Journal of Fluid Mechanics, vol. 664, pp. 313-336, 2010.